JAMES | Journal of Advances in Modeling Earth Systems

RESEARCH ARTICLE
10.1029/2021MS002715

Influence of Nonseasonal River Discharge on Sea Surface Salinity and Height

Hrishikesh A. Chandanpurkar[1,2,3], Tong Lee[1], Xiaochun Wang[4], Hong Zhang[1], Severine Fournier[1], Ian Fenty[1], Ichiro Fukumori[1], Dimitris Menemenlis[1], Christopher G. Piecuch[5], John T. Reager[1], Ou Wang[1], and John Worden[1]

[1]Jet Propulsion Laboratory, California Institute of Technology, Pasadena, CA, USA, [2]University of Saskatchewan, Saskatoon, SK, Canada, [3]FLAME University, Pune, India, [4]University of California Los Angeles, Los Angeles, CA, USA, [5]Woods Hole Oceanographic Institution, Woods Hole, MA, USA

Key Points:

- Nonseasonal discharge (deviation from seasonal climatology) has measurable impacts on model salinity and sea level near major rivers
- Inclusion of nonseasonal discharge leads to notable improvement of model-observation comparison near major river mouths
- A recent theory underpredicts the impact of discharge on sea level and has limited skill when applied to equatorial and Arctic rivers

Correspondence to:
T. Lee,
tlee@jpl.nasa.gov

Citation:
Chandanpurkar, H. A., Lee, T., Wang, X., Zhang, H., Fournier, S., Fenty, I., et al. (2022). Influence of nonseasonal river discharge on sea surface salinity and height. *Journal of Advances in Modeling Earth Systems*, *14*, e2021MS002715. https://doi.org/10.1029/2021MS002715

Received 16 JUL 2021
Accepted 7 JAN 2022

Author Contributions:
Conceptualization: Hrishikesh A. Chandanpurkar, Tong Lee, Xiaochun Wang
Data curation: Hrishikesh A. Chandanpurkar, Xiaochun Wang, Hong Zhang, Severine Fournier
Formal analysis: Hrishikesh A. Chandanpurkar, Xiaochun Wang, Hong Zhang
Funding acquisition: Tong Lee, John Worden
Investigation: Hrishikesh A. Chandanpurkar, Tong Lee, Xiaochun Wang, Hong Zhang, Ian Fenty, Ichiro Fukumori, Dimitris Menemenlis

Abstract River discharge influences ocean dynamics and biogeochemistry. Due to the lack of a systematic, up-to-date global measurement network for river discharge, global ocean models typically use seasonal discharge climatology as forcing. This compromises the simulated nonseasonal variation (the deviation from seasonal climatology) of the ocean near river plumes and undermines their usefulness for interdisciplinary research. Recently, a reanalysis-based daily varying global discharge data set was developed, providing the first opportunity to quantify nonseasonal discharge effects on global ocean models. Here we use this data set to force a global ocean model for the 1992–2017 period. We contrast this experiment with another experiment (with identical atmospheric forcings) forced by seasonal climatology from the same discharge data set to isolate nonseasonal discharge effects, focusing on sea surface salinity (SSS) and sea surface height (SSH). Near major river mouths, nonseasonal discharge causes standard deviations in SSS (SSH) of 1.3–3 practical salinity unit (1–2.7 cm). The inclusion of nonseasonal discharge results in notable improvement of model SSS against satellite SSS near most of the tropical-to-midlatitude river mouths and minor improvement of model SSH against satellite or in-situ SSH near some of the river mouths. SSH changes associated with nonseasonal discharge can be explained by salinity effects on halosteric height and estimated accurately through the associated SSS changes. A recent theory predicting river discharge impact on SSH is found to perform reasonably well overall but underestimates the impact on SSH around the global ocean and has limited skill when applied to rivers near the equator and in the Arctic Ocean.

Plain Language Summary River discharge is important to the physics and biogeochemistry of the ocean. While the effects of seasonal discharge on the ocean have been studied extensively, there is inadequate understanding about the impacts of nonseasonal discharge (the deviation from seasonal climatology) on the ocean. Here we use a daily varying global discharge data set to study the latter effects, focusing on sea surface salinity (SSS) and sea surface height (SSH). We used model sensitivity experiments to isolate the effects of nonseasonal discharge. It is found that nonseasonal discharge has measurable impacts on SSS and SSH near major river mouths. The inclusion of nonseasonal discharge leads to some improvements of the model ocean near major river mouths. We also assessed the skill of a recently proposed theory that predicts the impact of river discharge on SSH using the output from the model sensitivity experiments. The theory is found to predict the discharge-induced SSH variation relatively well in terms of temporal correlation. However, we identified several limitations in the theoretical prediction of the discharge-induced SSH variations, including the amplitude of the SSH variation and the applicability for rivers near the equator and in the Arctic Ocean.

1. Introduction

River discharge into the ocean influences a range of ocean properties and processes, such as salinity, ocean dynamics, marine biology and ecosystems, and biogeochemistry (e.g., Boano et al., 2014; Fournier, Lee, & Gierach, 2016; Garvine, 1995; Gierach et al., 2013; Hickey et al., 2010; Horner-Devine et al., 2015; Rabalais et al., 1999). Moreover, upper-ocean salinity stratification caused by river discharge can affect air-sea interaction through the effect of the so-called barrier layer (e.g., Sprintall & Tomczak, 1992), thereby modulating weather and climate variability (e.g., Balaguru et al., 2012; Reul, Fournier, et al., 2014; Vizy & Cook, 2010). The stratification within the river plumes of major tropical rivers such as the Amazon and Orinoco may affect summertime hurricane frequency and intensity (Reul, Quilfen, et al., 2014; Vizy & Cook, 2010), though the effectiveness

Methodology: Hrishikesh A. Chandanpurkar, Tong Lee, Xiaochun Wang, Hong Zhang
Project Administration: Tong Lee
Resources: Tong Lee, Dimitris Menemenlis
Software: Hrishikesh A. Chandanpurkar, Xiaochun Wang, Hong Zhang
Supervision: Tong Lee
Validation: Hrishikesh A. Chandanpurkar, Tong Lee, Xiaochun Wang, Hong Zhang
Visualization: Hrishikesh A. Chandanpurkar, Hong Zhang
Writing – original draft: Hrishikesh A. Chandanpurkar, Tong Lee, Xiaochun Wang
Writing – review & editing: Hrishikesh A. Chandanpurkar, Tong Lee, Xiaochun Wang, Hong Zhang, Severine Fournier, Ian Fenty, Ichiro Fukumori, Dimitris Menemenlis, Christopher G. Piecuch, John T. Reager, Ou Wang, John Worden

of this influence is still under active investigation (e.g., Hernandez et al., 2016; Newinger & Toumi, 2015). River discharge provides a major source of nutrients to the ocean and influences primary productivity in shelf ecosystems (e.g., Hickey et al., 2010). Nutrient-dense discharge can cause hypoxic conditions (e.g., Rabalais et al., 1999). By changing upper-layer density through salinity (halosteric effects), river discharge also impacts coastal sea level (e.g., Meade & Emery, 1971; Piecuch & Wadehra, 2020; Piecuch et al., 2018). For the US East and Gulf coasts, for example, 1 km^3 increase of annual discharge corresponds to 0.01–0.08 cm of increase in sea level (Piecuch et al., 2018).

While seasonal discharge is known to influence the ocean significantly (e.g., Fournier, Lee, & Gierach, 2016; Fournier et al., 2017; Piecuch & Wadehra, 2020), nonseasonal discharge (i.e., the deviation from seasonal climatology) can also cause significant responses in regional oceans. Such nonseasonal variability can occur on multiple timescales, including synoptic (days), intraseasonal (weeks to months), and interannual-to-decadal. There have been various regional studies focusing on the effects of nonseasonal discharges of different rivers on the physical state of regional oceans (e.g., Akhil et al., 2016; Dandapat et al., 2020; Durand et al., 2011; Fournier, Lee, & Gierach, 2016, Fournier, Reager, et al., 2016; Fournier et al., 2017; Gierach et al., 2013; Giffard et al., 2019; Han & Webster, 2002). In particular, nonseasonal discharge impacts on sea surface salinity (SSS) and sea surface height (SSH) can be as large as a few practical salinity unit (psu) and cm, respectively, as we discuss in the examples in the next paragraph to motivate the present study.

In the Gulf of Mexico, interannual variability of Mississippi River discharge was found to induce observed SSS anomalies of 3–4 psu near the river mouth, comparable to the magnitude of the seasonal cycle at that location (Fournier, Lee, & Gierach, 2016; Gierach et al., 2013). In 2016, runoff from the Texas shelf (a climatologically low-discharge region) induced by a severe storm caused a freshwater plume with observed SSS signal as large as that of the neighboring Mississippi River plume (Fournier, Reager, et al., 2016). The anomalous freshwater plume had a significant impact on the marine ecosystem in the northern Gulf of Mexico (Gittings, 2016). A modeling study by Dandapat et al. (2020) found a 2-psu SSS difference in the northern Bay of Bengal (BoB) between high- and low-discharge years. As far as SSH is concerned, a regional modeling study by Giffard et al. (2019) suggested that in addition to influencing the local SSH at the river mouth, Amazon discharge can induce 3.3 cm of remote SSH response in the Caribbean Archipelago. Piecuch et al. (2018) found that interannual-to-decadal variations of river discharge and observed SSH along the United States' East and Gulf Coasts are significantly correlated, with a 1-km^3 increase of annual river discharge corresponding to 0.01–0.08 cm of SSH rise depending on location. They further established an analytic theory to explain the causality of river discharge and SSH variations.

While there have been various regional studies for the effects of nonseasonal discharge, a global investigation has not yet been carried out. The only two global studies for river discharge effects (Piecuch & Wadehra, 2020; Sun et al., 2019) were for the impact of the seasonal climatology of discharge. One of the key reasons for this is the lack of up-to-date global discharge datasets that include nonseasonal variation.

Globally, discharge data availability has decreased since the 1980s due to management and financial constraints in operating the gauge network as well as an increased unwillingness of some countries in sharing hydrological data (Chandanpurkar et al., 2017; Durand et al., 2019). The only comprehensive gridded global discharge data set with interannually varying discharge estimates is from Dai et al. (2009), based on a curated relationship between observations and simulated discharge. The data set has not been updated in the past decade (Durand et al., 2019). To our best knowledge, all global ocean models and assimilation systems have been using seasonal climatology of river discharge because of the unavailability of a global river discharge data set that includes nonseasonal variations. As a result, the global model and assimilation products cannot properly represent the nonseasonal variability of SSS near major river plumes due to river discharge. For example, the state-of-the-art United States Navy operational ocean analysis system based on the Hybrid Coordinate Ocean Model fails to represent the interannual-to-decadal variation of SSS near some of the major river plumes, such as the Mississippi and Changjiang Rivers (e.g., Fournier, Lee, & Gierach, 2016; Wu et al., 2020). Near the Mississippi River mouth, the interannual-to-decadal SSS variation observed by satellites can reach 3–4 psu, which is as large as or larger than the magnitude of seasonal SSS at that location (Fournier, Lee, & Gierach, 2016). Some global ocean model and assimilation products are used to drive biogeochemical (BGC) models. The missing effect of nonseasonal discharge forcing in these products could adversely affect the fidelity of the BGC models, for example, because of the absence of the interannual-to-decadal variation of nutrient supply associated with nonseasonal river discharge and the related changes in upper-ocean stratification.

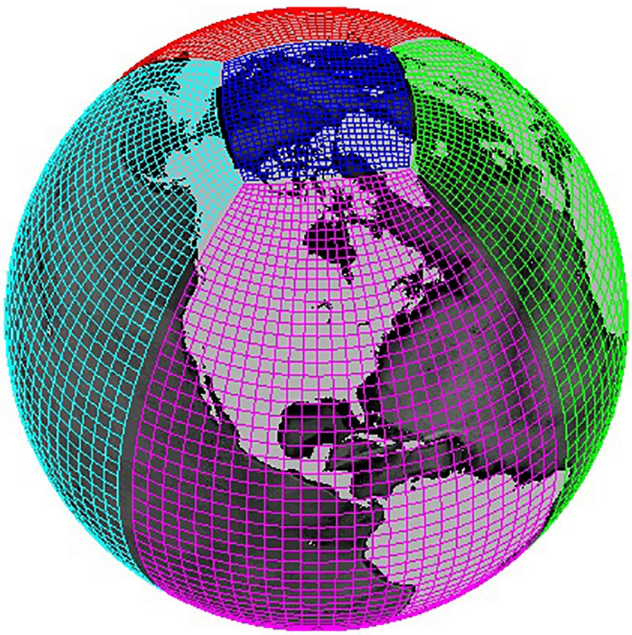

Figure 1. Illustration of the Lat-Lon-Cap (LLC) grid for the MITgcm model. The grid spacing shown is for LLC30, 9 times coarser than that of LLC270 that is too dense to present graphically.

Recently, a daily varying global river discharge product, with the intended use for driving ocean models, was produced by the Japanese 55-year atmospheric Reanalysis (JRA55) project (Tsujino et al., 2018). This product, referred to as the JRA55-drive ocean (JRA55-do, Suzuki et al., 2018), is a discharge data set that includes synoptic, intraseasonal, as well as interannual-to-decadal variations of river discharge around the global ocean. JRA55-do has a 0.25° spatial resolution along the coastlines of the global ocean, covering the period of 1958 to near present. This discharge data set provides the first opportunity to quantify the impacts of nonseasonal discharge around the global ocean. Such an assessment is the main objective of this study.

In this paper, we force a global ocean model with JRA55-do daily varying river discharge to quantify the effects of nonseasonal discharge on the ocean state near major river plumes. To isolate the effects of nonseasonal discharge, we conduct a second experiment with the ocean model forced by daily climatology from JRA55-do discharge while keeping the rest of the forcings identical to the first experiment. We then analyze the differences between the two model simulations in terms of SSS and SSH. The reasons for focusing on these variables as a starting point are: (a) these variables are directly affected by river discharge, and (b) global synoptic maps of these variables are available from satellite observations. We address three specific questions:

1. Does the inclusion of nonseasonal discharge have measurable (based on the accuracies of satellite observations) impacts on model SSS and SSH near major river plumes?
2. Does the inclusion of nonseasonal discharge improve the model state near major river mouths relative to satellite observations?
3. To what extent the impact on SSH can be inferred from SSS and river discharge?

In Section 2, we describe the datasets, the model, and the methods. We then present and discuss the results of the analysis to address the above questions. Specifically, in Section 3.1, we characterize the effects of nonseasonal discharge on SSS and SSH. In Section 3.2, we discuss whether these effects improve the comparison of the model with satellite observations of SSS and SSH. In Section 3.3, we explain the impact of nonseasonal discharge on SSH through a theoretical relation relating the changes in SSS and steric height; we also evaluate the skill of an existing, simplified theory for inferring the impacts of river discharge on SSH using river discharge estimates. The concluding section summarizes the findings, addresses the potential implications and caveats of the results, discusses future directions of further investigations.

2. Model, Data, and Methods

2.1. Model

The global ocean model used in this study is a global configuration of the Massachusetts Institute of Technology general circulation model (MITgcm; Marshall, Adcroft, et al., 1997, Marshall, Hill, et al., 1997) on a Latitude-Longitude-Cap (LLC) grid (Forget et al., 2015). The grid features a variable horizontal resolution of 12–30 km from the high-latitude to tropical oceans and is referred to as LLC270 (Figure 1). There are 50 vertical levels with depth increments ranging from 10 m in the upper ocean to 457 m in the abyss (Zhang et al., 2018). The model uses advanced mixing schemes, including an eddy kinetic energy parameterization for vertical mixing (Gaspar et al., 1990) and the Gent-and-McWilliams/Redi (GM/Redi) isopycnal mixing (Gent & Mcwilliams, 1990; Redi, 1982).

The surface forcings of the model include wind stress for the momentum equation, surface heat fluxes for the heat equation, and surface freshwater flux (evaporation minus precipitation) for the continuity equation, which is also forced by river discharge. Surface freshwater flux and river discharge are implemented as natural freshwater boundary conditions where the top-layer salinity decreases (increases) in response to the addition (removal) of freshwater volume. The natural freshwater boundary condition conserves salt in the ocean.

Our model experiments leverage upon an optimized solution of the LLC270 model for the 1992–2017 period constrained by multi-platform *in-situ* and satellite observations of the ocean, including marine surface meteorological measurements. The optimization was based on the state and parameter estimation procedure described in Forget et al. (2015) for the Estimating the Circulation and Climate of the Ocean (ECCO) Version-4 (V4) product. ECCO V4 used a MITgcm global-ocean configuration with a nominal 1° horizontal grid spacing, as opposed to the nominal 1/3° grid of LLC270. The adjoint method (e.g., Wunsch & Heimbach, 2013; Wunsch et al., 2009) is used to adjust a set of control variables: initial temperature and salinity conditions, surface atmospheric conditions, and time-mean, three-dimensional background mixing coefficients for vertical diffusivity and GM/Redi along-isopycnal and isopycnal-thickness diffusivities. The control variables are adjusted via an iterative optimization procedure from first-guess (iteration 0) values to improve the fit of the model solution to observations during the 1992–2017 period. It is important to note that the model solution always satisfies the model equations despite the adjustment of the initial state, surface forcings, and time-mean background mixing coefficients.

For the present study, we perform forward model experiments using the optimized control variables obtained after 50 adjoint-method iterations. Further description of the LLC270 optimization and a detailed evaluation of the iteration-50 LLC270 optimized solution is available in Zhang et al. (2018). The relatively large GM/Redi background coefficients used (e.g., hundreds of m^2/s over much of the model ocean) suppressed mesoscale variability significantly, thus limiting active eddying activity primarily to few regions such as open-ocean areas near the Gulf Stream and tropical Pacific instability waves as well as the Leeuwin Current off western Australia. These regions, far away from major river mouths, will not be discussed in this study.

Until now, the default river discharge forcing in the LLC270 model was based on an estimated seasonal climatology (Fekete et al., 2002). Therefore, the influence of nonseasonal discharge has not been accounted for. As discussed in Section 1, this is common for the global ocean model and assimilation products. Furthermore, in the default configuration of the LLC270 model, the river discharge was spread out over hundreds of km around the river mouths using a smoothing operator, a procedure inherited from the lower-resolution ECCO models that have difficulty in dispersing the riverine waters away from the coasts and in maintaining computational stability (Piecuch & Wadehra, 2020). These have been significant limitations of the model in representing the effects of river discharge in the ocean (e.g., the spatial structure of the river plumes).

Here we introduce daily discharge from the JRA55-do data set (Suzuki et al., 2018) as the discharge forcing to the global ocean. This data set is the discharge component of Japanese 55-year atmospheric Reanalysis product (JRA55) for driving ocean-sea-ice models (JRA55-do, Tsujino et al., 2018). The JRA55-do discharge data set routed the land surface runoff estimated from JRA55-do data to the coastlines to produce river discharge while applying several methods to remove biases in the discharge estimates to provide a better comparison with Dai et al. (2009). The Dai et al. (2009) discharge data set has been used as a standard discharge forcing for ocean models within the framework of the Coordinated Ocean-Ice Reference Experiments (CORE; Large & Yeager, 2009). This discharge data set is now being replaced by JRA55-do discharge, which is also the standard discharge forcing for the Ocean Model Intercomparison Project Phase 2 project (Tsujino et al., 2020). Overall, the JRA55-do discharge data compare reasonably well with available river gauge data around the world ocean (Suzuki et al., 2018). We implement the JRA55-do river discharge by interpolating the 0.25°-resolution discharge estimates along the coastlines onto the coastlines of the LLC270 model grid without using a smoothing operator to spread the river discharge influence away from the coasts, similar to what was done in Dandapat et al. (2020) and Feng et al. (2021).

2.2. Data

We compare model SSS and SSH with both satellite observations and *in-situ* measurements. For satellite observations, we use the Level-3 debiased version-4 SMOS SSS product from the Centre Aval de Traitement des Donnees SMOS (CATDS; Boutin et al., 2018). This data set provides 9-day running-average SSS maps on a 25-km grid (with a smoothing scale of 70 km) from January 2010 to September 2019. We also use the Level-3 version-4.2 SMAP SSS product distributed by the Jet Propulsion Laboratory (JPL), with 8-day running-average maps on a 0.25° grid that have smoothing scales of 55–60 km (Fore et al., 2016) for the period of April 2015 to present. To compare model SSH with observations, we use the Level-4 SSH anomalies obtained from multiple satellite altimeters. This data set, provided on a 0.25° grid for the period from 1993 to the present, is produced by the Copernicus Marine Environment Monitoring Service. The information about the smoothing scales of this

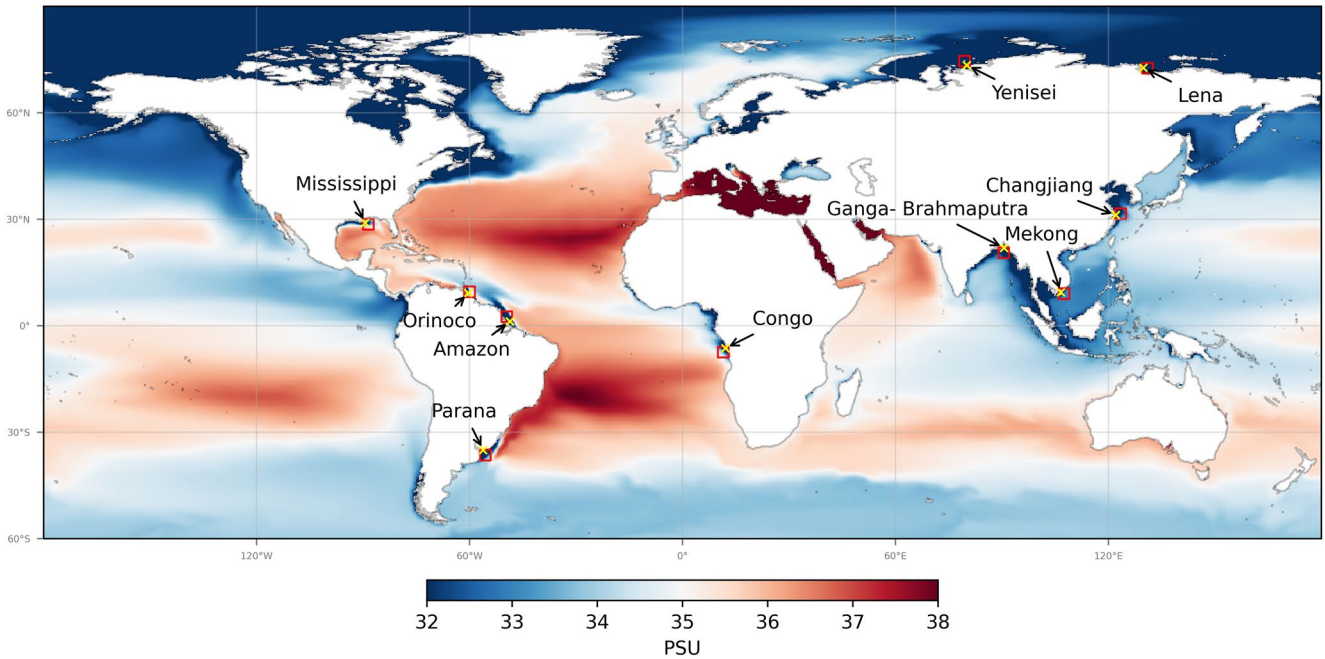

Figure 2. Geographical locations of the mouths of the 10 largest rivers as well as 3° × 3° boxes near the river mouths studied in this paper. The color map shows the time-mean SSS simulated by the model.

data set is not available. However, the effective wavelengths resolvable by these maps were estimated to be 800, 200, and 100 km in, respectively, the equatorial, mid-latitude, and high-latitude oceans (Ballarotta et al., 2019). The effective de-correlation scales would be 200, 50, and 25 km, respectively.

2.3. Methods

We conduct two experiments using LLC270 forward model for the period 1992–2017. The surface forcings for these two experiments are obtained from the optimized surface forcings from the LLC270 50th-iteration optimization, implemented as prescribed surface flux forcings that are identical for the two forward model experiments. However, the discharge forcing for the two experiments is different. The first experiment is forced with the total daily JRA55-do discharge, which includes seasonal as well as nonseasonal variability. This experiment is denoted as *tot*. The second experiment is forced with seasonal climatological discharge from JRA55-do, computed by averaging the discharge for any particular day of the year over different years during 1992–2017. This experiment is denoted as *clm*. The model outputs are stored at 5-day intervals.

The analysis focuses primarily on the difference between the two experiments in their nonseasonal SSS and SSH variations (referenced to the respective seasonal cycle) near the mouths of the 10 largest rivers by discharge volume. Figure 2 shows the names of these rivers and the locations of the river mouths, The difference in nonseasonal SSS and SSH between the two experiments are denoted as $\Delta SSS = SSS_{tot} - SSS_{clm}$ and $\Delta SSH = SSH_{tot} - SSH_{clm}$, respectively. We also denote the detrended nonseasonal discharge as ΔQ. The nonseasonal anomalies are further separated into intraseasonal and interannual-to-decadal anomalies using a 13-month filter. For the latter time scales, the statistics presented in the paper are dominated by interannual time scales.

Since the initial state and surface forcings for the two experiments are identical, the differences between the *tot* and *clm* experiments in terms of ΔSSS and ΔSSH are due to the presence (absence) of nonseasonal discharge forcing ΔQ as well as the difference in internal variability such as mesoscale instability that is partially admitted by the relatively coarse-resolution model. As mentioned in Section 2.1, however, mesoscale variability is not active in much of the model ocean including near major river mouths because of the coarse model resolution and large mixing coefficients. The results presented in the next section also suggest that the effect of nonseasonal discharge is the dominant factor causing ΔSSS and ΔSSH near major river mouths. This is evidenced by (a) the coherence among ΔQ, ΔSSS and ΔSSH (Section 3.1), (b) notable improvements of nonseasonal SSS with respect

to satellite SSS near several major river mouths and of SSH against tide gauge data near the Mississippi River mouth when nonseasonal discharge is included (Section 3.2), and (c) the good skill of using ΔQ to predict ΔSSH consistent with theory (Section 3.3).

3. Results and Discussion

3.1. Impacts of Nonseasonal Discharge

In this section, we address the first question of this study, namely, whether the inclusion of nonseasonal discharge has measurable impacts on model SSS and SSH near major river plumes. "Measurable" here refers to whether the magnitudes of ΔSSS (or ΔSSH; as defined in Section 2.3) exceed the uncertainties of satellite-derived SSS (or SSH) products. If ΔSSS and ΔSSH are measurable relative to the observational uncertainties, there is a potential to use the observed SSS and SSH fields to determine if the model simulation forced by daily discharge (i.e., the *tot* experiment) improves upon that forced by climatological discharge (i.e., the *clm* experiment).

In tropical to mid-latitude oceans, the average uncertainties of satellite SSS products averaged on a 1° grid and monthly time scales range from somewhat less than 0.2 psu to approximately 0.3 psu, depending on the product, with the uncertainty of the Aquarius SSS (Lee, 2016) being somewhat smaller than those from the SMAP (Meissner et al., 2019) and SMOS (Boutin et al., 2018) satellites on the 1° and monthly scales. The aforementioned estimates of satellite SSS uncertainties also include the poorly known sampling and mapping errors of the in-situ salinity products used to evaluate the satellite SSS on these scales (Boutin et al., 2016). In polar oceans, the uncertainty of satellite SSS is a few times larger because of the poor sensitivity of the L-band radiometry to salinity when sea surface temperature is lower than 5°C (Fournier et al., 2019; Tang et al., 2018; Vinogradova et al., 2019). If one considers SSS variations only (i.e., excluding time-mean biases), the uncertainties of satellite SSS are smaller, especially for nonseasonal variations (i.e., excluding the seasonal cycles). For example, the averaged upper-bound uncertainty estimate for Aquarius SSS is 0.16 (0.1) psu for temporal (nonseasonal) variations, with the uncertainty estimates reducing further when averaging beyond the 1° spatial scale (Lee, 2016). The uncertainties for nonseasonal variations are the most relevant to our study.

In coastal oceans, the uncertainties of satellite SSS products are expected to be larger because of the potential contamination of the SSS retrievals by land signal leakage. In-situ sampling in such regions is typically insufficient to provide a reliable assessment of satellite SSS uncertainties and to correct the effect of land contamination on SSS retrievals (Boutin et al., 2016; Vinogradova et al., 2019). Therefore, satellite SSS within one footprint of the coasts (e.g., approximately 100 km for Aquarius and 40 km for SMOS and SMAP) are typically masked out.

For SSH, the average standard error of the gridded SSH product based on multiple satellite altimeter missions is 2–3 cm (https://climatedataguide.ucar.edu/climate-data/aviso-satellite-derived-sea-surface-height-above-geoid). However, the uncertainties of altimetric SSH near the coasts are significantly larger than the average uncertainties over open ocean (e.g., Vignudelli et al., 2019). Moreover, coastal altimetric SSH uncertainty is regionally dependent because the retrieval involves specific geophysical processes and correction issues that may be significantly different from one coastal region to another (see review by Vignudelli et al., 2019). Evaluations of coastal altimetric SSH using tide-gauge observations showed discrepancies ranging from a few cm to tens of cm depending on the location. For example, Dieng et al. (2019) found approximately 4–5 cm of root-mean-square error (RMSE) for a gridded merged altimetry product at the African coast of the southeast tropical Atlantic. Marcello et al. (2021) reported about 4–12 cm of RMSE for SSH measurements from various altimeter missions at the Baltic coast. Vu et al. (2018) documented 8 to tens of cm of RMSE for altimetric SSH measurements at the French Atlantic coast.

Figure 3 illustrates two diagnostic quantities related to ΔSSS for nine domains encompassing the 10 major river mouths, with a large domain enclosing the Amazon and Orinoco river plumes (Figures 3a and 3b). The two diagnostics quantities are presented for each domain in a pair of panels. The first quantity is the temporal standard deviation of ΔSSS (presented on the left of each pair such as Figures 3a, 3c and 3e, etc.) at each location, denoted as σ(ΔSSS). This quantity reflects the overall impact of nonseasonal discharge ΔQ on nonseasonal SSS (assuming the difference in mesoscale instability between the two runs to be small). The second quantity is the maximum absolute value of ΔSSS (presented on the right of each pair such as Figures 3b, 3d and 3f, etc.) at each location, denoted as max(|ΔSSS|). To compute max(|ΔSSS|), the time series of two model runs are first differenced at each location, then the maximum absolute value of the ΔSSS time series through the entire period is determined.

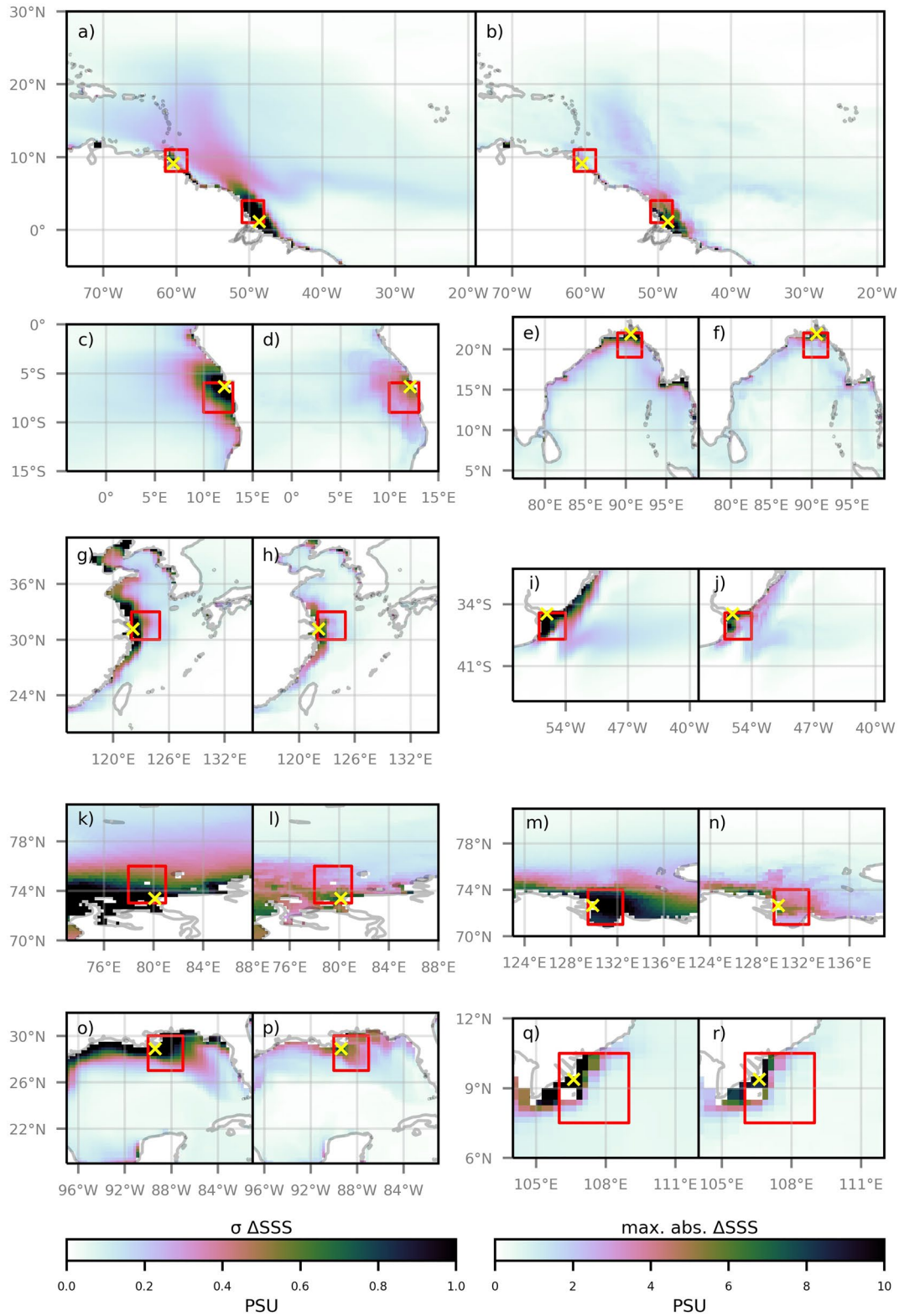

Figure 3. Temporal standard deviation of nonseasonal sea surface salinity (SSS) differences between the *tot* and *clm* experiments (i.e., ΔSSS) (left-hand-side of each two-panel pair) and the maximum absolute difference for the ΔSSS (right-hand-side of each two-panel pair) for regional domains encompassing the major river mouths: Amazon and Orinoco (a), (b), Congo (c), (d), Ganges-Brahmaputra (e), (f), Changjiang (g), (h), Parana (i), (j), Yenisei (k), (l), Lena (m), (n), Mississippi (o), (p), and Mekong (q), (r).

While σ(ΔSSS) provides an assessment of the overall impact through times, max(|ΔSSS|) can highlight the large impacts of some infrequent events (e.g., on synoptic or interannual time scales) that may not stand out in σ(ΔSSS). The patterns of max(|ΔSSS|) are generally similar to those of σ(ΔSSS). While the typical values of σ(ΔSSS) near major river mouths are close to 1 psu, the maximum values of max(|ΔSSS|) can be 10 times larger due to the impacts of particular discharge events.

The patterns of σ(ΔSSS) associated with the Amazon-Orinoco Rivers (Figure 3a) and Congo River (Figure 3c) extend relatively far away from the river mouths. For example, σ(ΔSSS) values of 0.2 psu or larger can reach a thousand km or more into the interior of the tropical Atlantic ocean, as well as into the Caribbean for the case of the Amazon-Orinoco Rivers. The relatively large spatial extent of σ(ΔSSS) away from the mouths of the Amazon-Orinoco and Congo Rivers is consistent with existing knowledge about the effects of regional ocean circulations that spread the influence of these rivers (Chao et al., 2015; Giffard et al., 2019). The patterns of σ(ΔSSS) associated with the Parana River (Figure 3i) and that near the Mississippi River (Figure 3o) also have values of σ(ΔSSS) extending hundreds of km into the interior ocean along the respective river plume. For the rest of the domains, the patterns of σ(ΔSSS) extend predominantly along the coasts.

The BoB, significantly influenced by the large Ganges-Brahmaputra River system, is discussed here as a particular example because of several relevant previous studies, including one that performed a model sensitivity experiment as the present study but with a regional model. In the BoB (Figure 3e), σ(ΔSSS) values of 0.2 psu or more are confined to the northern BoB (north of 10°N). However, weaker signals extend around the southern tip of India into the southeast Arabian Sea. This is because during certain years the riverine waters carried by the East India Coastal Current reach further south and subsequently into the southeast Arabian Sea. Both of these aspects are consistent with existing knowledge (e.g., Akhil et al., 2016; Durand et al., 2011). The years with strong negative Indian Ocean Dipole (IOD) events are often associated with a more southward extension of the freshwater plume along the southeast coast of India because of the remote wind forcings associated with IOD (e.g., Dandapat et al., 2020; Fournier et al., 2017). Similar to our global study, Dandapat et al. (2020) conducted regional model sensitivity experiments where they contrasted two simulations forced by daily JRA55-do discharge and its seasonal climatology, respectively. They found that the composite SSS difference between the two model runs during July-December (the months following monsoon-induced discharge) of four high-discharge years (1980, 1988, 1990, 2007) differ from that during four low-discharge years (1979, 1986, 1992, 2009) by as much as 2 psu in the northern BoB and off the southeast coast of India.

To provide a relevant comparison with the results by Dandapat et al. (2020), we present in Figure 4 the ΔSSS during July–December of 1998 and 2007 (high-discharge years) and 1992 and 2009 (low-discharge years). The years 1992, 2007, and 2009 were part of the composite analysis by Dandapat et al. (2020). The year 1998 was discussed by Durand et al. (2011) as a high-discharge year that resulted in the freshwater plume reaching the southeast Arabian Sea. Figure 4 shows that the difference in ΔSSS magnitudes between the high- and low-discharge years can indeed be close to 2 psu. This is consistent with the finding of Dandapat et al. (2020), despite the fact that the patterns seen in Figure 4 have no eddy patterns (different from Figure 6 of Dandapat et al., 2020) because of the lower resolutions of our model as well as the relatively large GM/Redi mixing coefficients.

The values of σ(ΔSSS) and max(|ΔSSS|) at the river mouth locations of the world's 10 largest rivers (by discharge volume) are presented in Table 1. The σ(ΔSSS) at these river mouths range from 1.3 to 3 psu while the max(|ΔSSS|) values range from 5.2 to 13.4 psu. The values of σ(ΔSSS) and max(|ΔSSS|) shown in Table 1 are at the model grid points closest to the river mouths. Satellite SSS at locations so close to the coasts is typically masked-out, as mentioned earlier. In-situ measurements at such locations are either not available or have insufficient sampling to assess the model. We, therefore, computed the averages of ΔSSS, averaged over 3° × 3° near the river mouths. The corresponding σ(ΔSSS) and max(|ΔSSS|) are shown in Table 2. The values range from 0.2 to 0.9 psu for σ(ΔSSS) and 0.5 to 3.1 psu for max(ΔSSS). Fournier and Lee (2021) reported that the average discrepancy between SMOS and SMAP SSS anomalies within 3° × 3° of major river mouths from the tropics to mid-latitudes is approximately 0.3 psu. For nonseasonal SSS anomalies, however, the averaged discrepancy is approximately 0.2 psu. Therefore, the statistics shown in Table 2 are overall comparable or larger than the uncertainties of satellite-based nonseasonal SSS averaged over 3° × 3°.

The regions with pronounced ΔSSS near river plumes are also associated with increased ΔSSH, as shown in Figure 5, which is a similar presentation as Figure 3 but for σ(ΔSSH) and max(|ΔSSH|). The overall similarity

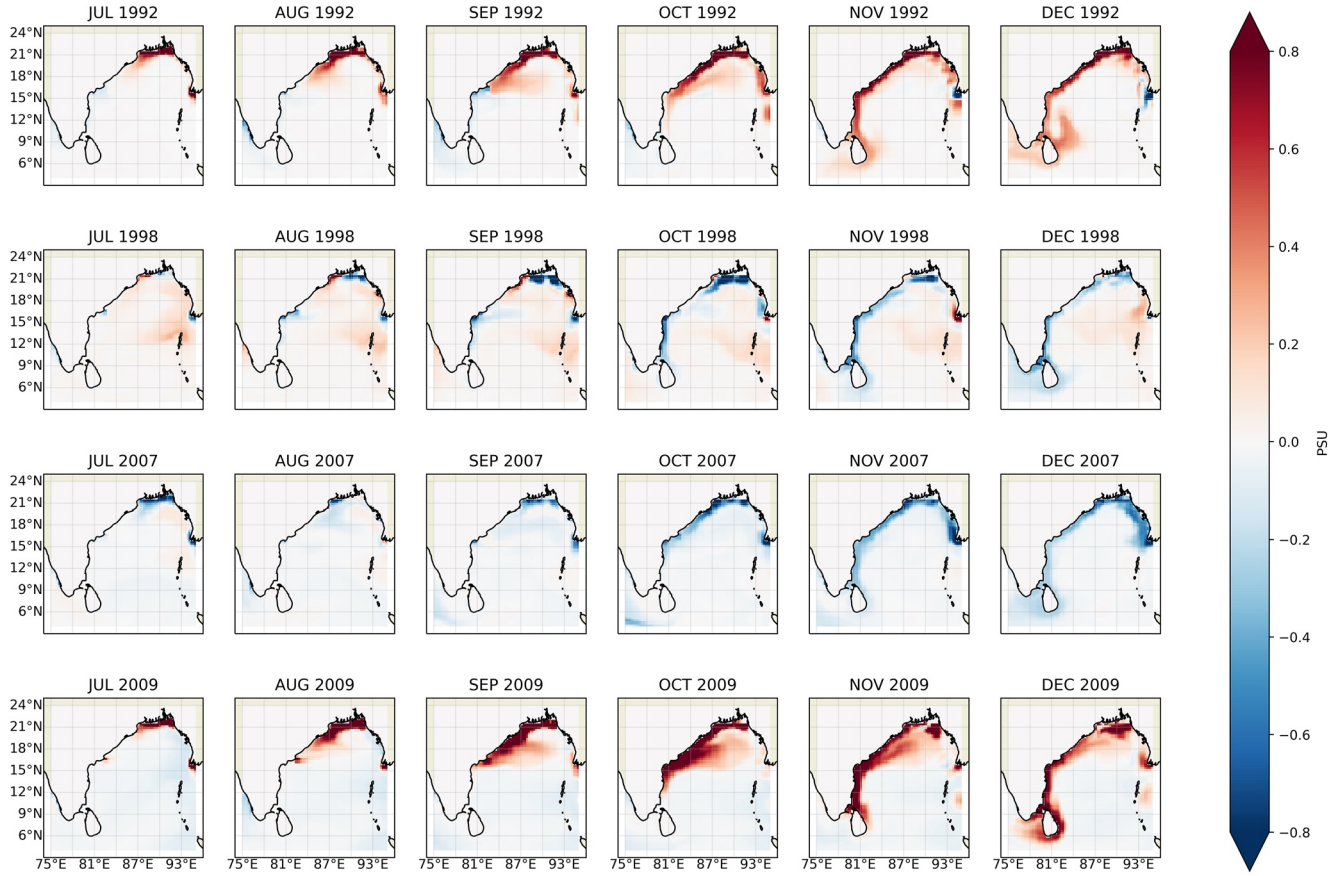

Figure 4. The difference in sea surface salinity between the *tot* and *clm* experiments (in psu) during July–December of 1992, 1998, 2007, and 2009. The years 1998 and 2007 (1992 and 2009) are associated with anomalously high (low) discharge of the Ganges-Brahmaputra River. The range of the color scale is chosen to be the same as Figure 6 in Dandapat et al. (2020).

between the patterns of σ(ΔSSS) shown in Figure 3 and σ(ΔSSH) shown in Figure 5 is indicative of the halosteric effect on SSH. The σ(ΔSSH) values near the mouths of several major rivers (Table 1) are comparable to the 2–3 cm average standard error of the gridded SSH product based on multiple satellite altimeter missions

Table 1
Statistics of ΔSSS and ΔSSH at River Mouth Locations of World's Ten Largest Rivers (by Discharge)

		ΔSSS (psu)		ΔSSH (cm)	
	Mouth coordinates (longitude, latitude)	Standard deviation	Maximum absolute	Standard deviation	Maximum absolute
Amazon	48.625°W, 1.125°N	2.5	11.7	1.9	8.8
Congo	12.125°E, 6.375°S	2.4	9.8	2	7.4
Orinoco	60.375°W, 9.125°N	1.4	8.5	1.2	5.5
Ganges-Brahmaputra	90.625°E, 21.875°N	1.4	9.6	1	5.0
Changjiang	122.125°E, 31.125°N	2.7	12.5	1.9	7.0
Parana	56.125°W, 35.125°S	3.0	11.8	2.7	8.8
Yenisei	80.125°E, 73.375°N	1.6	7.5	2.0	7.6
Lena	129.875°E, 72.625°N	1.3	5.2	1.5	5.9
Mississippi	89.375°W, 28.875°N	2.4	8.1	2.3	8.3
Mekong	106.625°E, 9.375°N	2.5	13.4	1.3	5.5

Table 2
Same as Table 1, but for ΔSSS and ΔSSH Averaged Over 3° × 3° Regions Near the River Mouths

		ΔSSS (psu)		ΔSSH (cm)	
	Box coordinates (longitude extent; latitude extent)	Standard deviation	Maximum absolute	Standard deviation	Maximum absolute
Amazon	48–51°W; 1–4°N	0.8	3.1	0.8	3.0
Congo	10–13°E; 6–9°S	0.6	2.7	0.8	2.9
Orinoco	58.5–61.5°W; 8–11°N	0.2	0.8	0.4	1.7
Ganges-Brahmaputra	89–92°E; 19–22°N	0.3	1.4	0.5	1.4
Changjiang	122–125°E; 30–33°N	0.6	2.1	0.6	2.1
Parana	54–57°W; 35–38°S	0.9	3	0.9	2.8
Yenisei	78–81°E; 73–76°N	0.6	2.0	1.0	3.0
Lena	129.5–132.5°E; 71–73°N	0.7	2.1	0.8	2.4
Mississippi	87–90°W; 27–30°N	0.6	2.2	0.9	2.5
Mekong	106–109°E; 7.5–10.5°N	0.2	0.9	0.4	1.2

(https://climatedataguide.ucar.edu/climate-data/aviso-satellite-derived-sea-surface-height-above-geoid) but is expected to be smaller than the uncertainties of coastal altimetric SSH. The max(|ΔSSH|) values at the mouths of the top 10 largest rivers range from 5.0 to 8.8 cm (Table 1). Because coastal altimetric SSH at the river mouths is subject to much larger uncertainties, we also present in Table 2 the values of σ(ΔSSH) and max(|ΔSSH|) for ΔSSH averaged over 3° × 3° near the river mouths. The magnitudes of the resultant σ(ΔSSH) are now less than 1 cm while those of max(|ΔSSH|) range from 1 to 3 cm. If one assumes the average error of open-ocean altimetric SSH (2–3 cm) to be random and uncorrelated among different 0.25° grid points of the merged altimetry product, the standard error of altimetric SSH averaged over 3° × 3° would be approximately 0.2–0.3 cm. These lower-bound estimates of errors are smaller than most of the values of σ(ΔSSH) and max(|ΔSSH|) shown in Table 2. However, the actual uncertainties of 3° × 3° averages of altimetric SSH near the river mouths, not well-documented, are expected to be larger because of correlated errors within 3° × 3° of the coasts.

It is of interest to compare the magnitude of ΔSSS (ΔSSH) with that of nonseasonal SSS_{tot} (SSH_{tot}) itself. While the former includes effects of nonseasonal discharge and intrinsic ocean variability, the latter also involves the effects of nonseasonal atmospheric forcing including the direct effect of nonseasonal atmospheric forcing on SSS (SSH) and the impact of ocean circulation variability driven by nonseasonal atmospheric forcing on SSS (SSH). As mentioned in Section 2.1 and further demonstrated in the rest of the paper, intrinsic ocean variability is not a dominant factor controlling SSS and SSH near river mouths in our model. Therefore, the ratio of magnitudes between ΔSSS (ΔSSH) and nonseasonal SSS_{tot} (SSH_{tot}) provides an indication of the relative importance of nonseasonal discharge effect and nonseasonal atmospheric forcing effect. In Figure 6, the left-hand-side of each two-panel pair shows the percentage ratio between the standard deviation of ΔSSS and that of nonseasonal SSS_{tot}: $R_\sigma(SSS) = \sigma(\Delta SSS)/\sigma(nonseasonal\ \ SSS_{tot}) \times 100$. The right-hand-side of each two-panel pair presents $\sigma(nonseasonal\ \ SSS_{tot})$ for reference. Figure 7 is a similar presentation but for $R_\sigma(SSH) = \sigma(\Delta SSH)/\sigma(nonseasonal\ \ SSH_{tot}) \times 100$ and $\sigma(nonseasonal\ \ SSH_{tot})$. The smaller the value of $R_\sigma(SSS)$ or $R_\sigma(SSH)$, the smaller the effect of nonseasonal discharge relative to the effect of nonseasonal atmospheric forcing.

The values of $R_\sigma(SSS)$ (Figure 6) are generally over 50% near most major river mouths. A notable exception is near the mouths of the Ganges-Brahmaputra River system, where the values of $R_\sigma(SSS)$ are less than 30%. It indicates that, near the Ganges-Brahmaputra river mouths, the effect of nonseasonal discharge on SSS is not as strong as the effect of nonseasonal atmospheric forcings, compared to other major river mouths. The values of $R_\sigma(SSH)$ (Figure 7) near major river mouths are substantially smaller than those of $R_\sigma\ \ (SSS)$. For example, near the Amazon River mouth, the values of $R_\sigma(SSH)$ are about 30% or less while those of $R_\sigma(SSS)$ are over 50%. It suggests that nonseasonal SSH is much more dominated by the effect of atmospheric forcing than by the effect of river discharge compared to the case for nonseasonal SSS. This makes it more challenging to improve

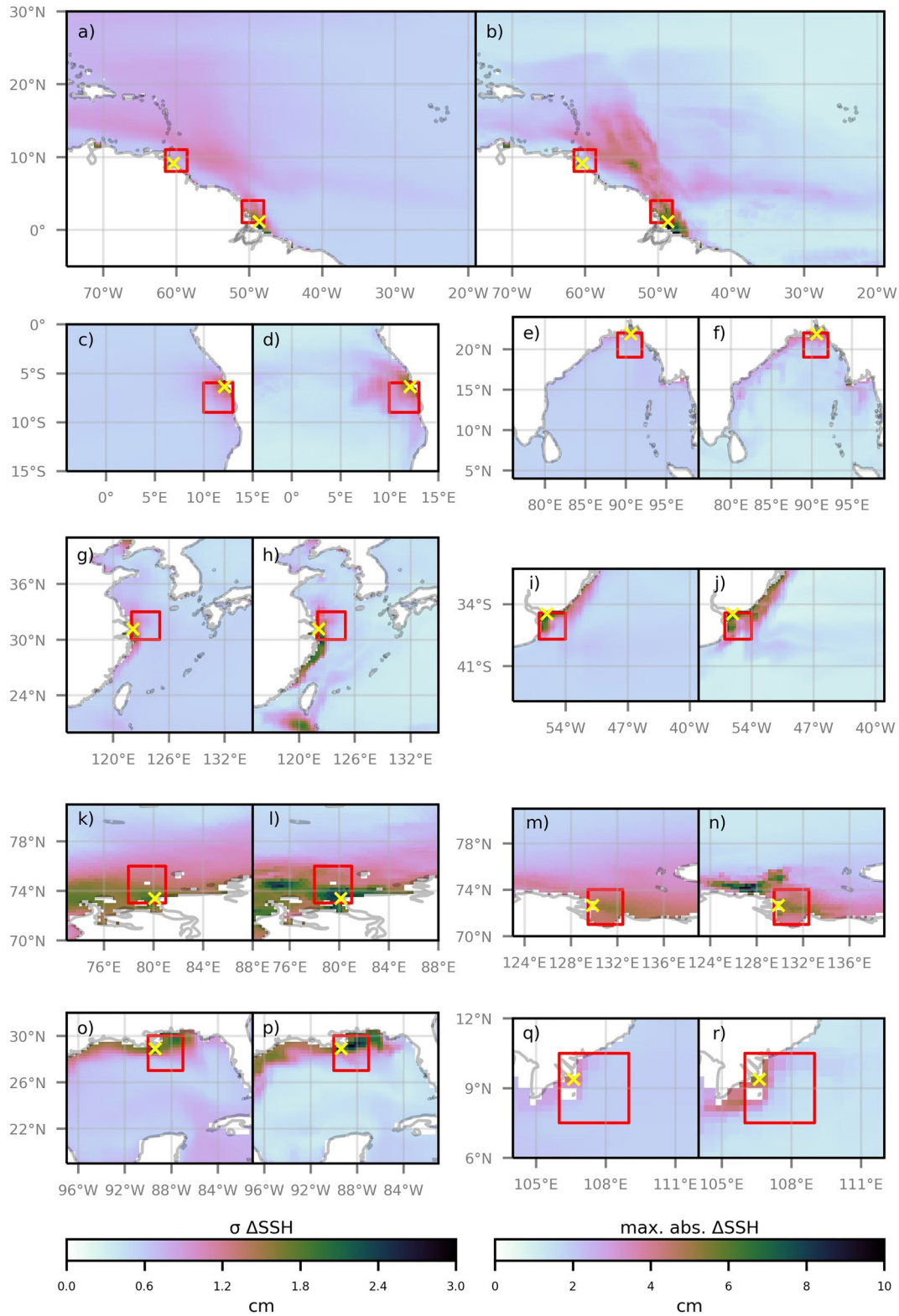

Figure 5. Temporal standard deviation of nonseasonal sea surface salinity (SSH) differences between the *tot* and *clm* experiments (i.e., ΔSSH) (left-hand-side of each two-panel pair) and the maximum absolute difference for the ΔSSH (right-hand-side of each two-panel pair) for regional domains encompassing the major river mouths: Amazon and Orinoco (a), (b), Congo (c), (d), Ganges-Brahmaputra (e), (f), Changjiang (g), (h), Parana (i), (j), Yenisei (k), (l), Lena (m), (n), Mississippi (o), (p), and Mekong (q), (r).

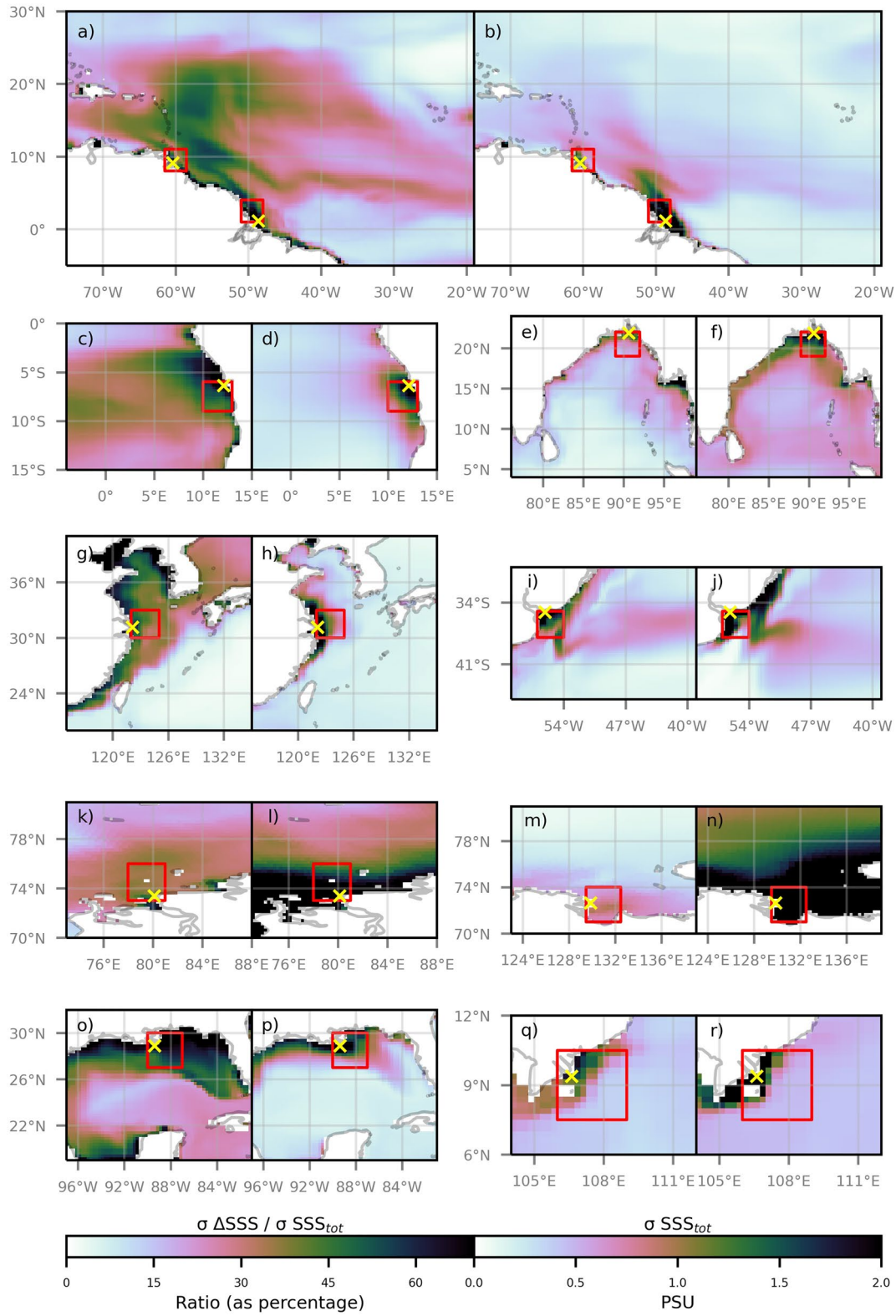

Figure 6. Percentage ratio between the standard deviation of ΔSSS and that of nonseasonal SSS_{tot} (left-hand-side of each two-panel pair), and the standard deviation of nonseasonal SSS_{tot} (right-hand-side of each two-panel pair) for regional domains encompassing the major river mouths: Amazon and Orinoco (a), (b), Congo (c), (d), Ganges-Brahmaputra (e), (f), Changjiang (g), (h), Parana (i), (j), Yenisei (k), (l), Lena (m), (n), Mississippi (o), (p), and Mekong (q), (r).

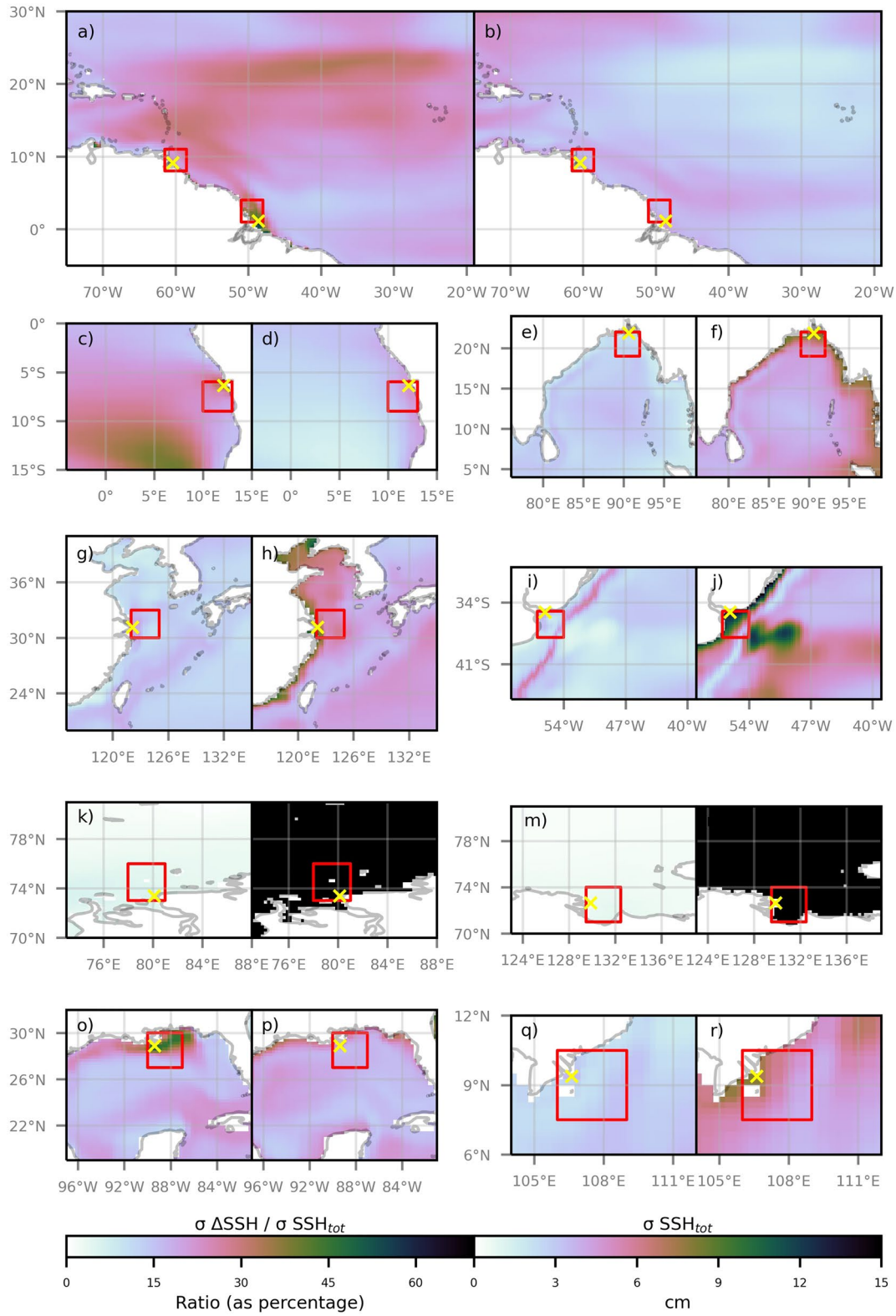

Figure 7. Percentage of the ratio between the standard deviation of ΔSSH and that of nonseasonal SSH_{tot} (left-hand-side of each two-panel pair), and the standard deviation of nonseasonal SSH_{tot} (right-hand-side of each two-panel pair) for regional domains encompassing the major river mouths: Amazon and Orinoco (a), (b), Congo (c), (d), Ganges-Brahmaputra (e), (f), Changjiang (g), (h), Parana (i), (j), Yenisei (k), (l), Lena (m), (n), Mississippi (o), (p), and Mekong (q), (r).

model SSH than to improve model SSS near river mouths by including nonseasonal discharge, as we illustrate in Section 3.2.

Giffard et al. (2019) reported that the Amazon discharge explained 12% of the nonseasonal variance of SSH in the Caribbean in their regional model. In our model simulations, ΔSSH explains only less than 10% of the nonseasonal SSH_{tot} variance in the Caribbean. The difference is likely due to the somewhat lower horizontal resolution and much lower vertical resolution of our model and the relatively large mixing coefficients.

We further analyze the relationship among nonseasonal discharge (ΔQ), the tendency of ΔSSS (i.e., d(ΔSSS)/dt), ΔSSS, and ΔSSH. Table 3 shows the analysis for the model's ocean grid points at the mouths of the 10 largest rivers. The coordinates of these river mouth locations are shown in row #1 of Table 3. The mixed-layer budget equation for ΔSSS (assumed to be representative of the difference in nonseasonal variation of mixed-layer salinity between the two runs) can be expressed as:

$$\frac{d(\Delta SSS)}{dt} = -\frac{\Delta Q \times S_0}{H \times A} + ocean\ \ dynamics \tag{1}$$

where S_0 is mean salinity, H is the mixed-layer depth, and A is the horizontal area of a model grid cell. The first term on the right-hand side is the nonseasonal river discharge effect. The second term on the right-hand side is the contribution of ocean dynamics (e.g., advection and mixing). Were ΔQ the only factor influencing ΔSSS (i.e., without ocean dynamics effect), ΔQ would have a strong anti-correlation with d(ΔSSS)/dt because an increase in river discharge would decrease SSS in time. We, therefore, first compute the correlation between ΔQ and d(ΔSSS)/dt. Table 3 shows that these two variables are actually poorly correlated (row #2). This indicates the importance of ocean dynamics, for example, in redistributing the ΔQ input. On the other hand, the correlation between ΔQ and ΔSSS (row #3) is much higher. Strong anti-correlation is also found between ΔSSS and ΔSSH (row #4), which we attributed to the halosteric effect on SSH in Section 3.3. As a result, ΔQ and ΔSSH also have a strong correlation (row #5). Similar analyses are performed for intraseasonal and interannual timescales. The results are shown in rows #6–9 and row #10–13, respectively. The conclusions for these timescales are similar to those for nonseasonal timescales in terms of the poor correlation between ΔQ and d(ΔSSS)/dt, and good correlations among ΔQ, ΔSSS, and ΔSSH.

As a graphic example to illustrate the results presented in Table 3, Figure 8 shows the time series comparison for ΔQ, −ΔSSS, and ΔSSH at a grid point near the Mississippi River mouth, for nonseasonal (Figure 8a), intraseasonal (Figure 8b), and interannual-to-decadal (Figure 8c) timescales. The good correlation among these three variables on the three timescales is obvious. Even on multi-decadal time scales, the small negative trend in ΔQ corresponds to similarly small negative trends in −ΔSSS and ΔSSH. Figure 8 also suggests that, for this location, the magnitudes of intraseasonal and interannual ΔSSS are similar. The same is true for ΔSSH. In other words, intraseasonal and interannual variations of the Mississippi River discharge have comparable effects on SSS (and SSH) on these two timescales.

The reason that ΔQ has poor relations with d(ΔSSS)/dt and d(ΔSSH)/dt is because of the contribution of ocean dynamics term on the right-hand-side of Equation 1. This ocean dynamics contribution is unlikely to be dominated by mesoscale instability. Were ΔSSS (or ΔSSH) dominated by the effect of mesoscale instability that is decoupled from nonseasonal discharge, we would not have found the coherence between ΔQ and ΔSSS (or ΔSSH). In fact, Piecuch et al. (2018) also found that the observed variations of river discharge are significantly correlated with SSH but not with SSH tendency on interannual-to-decadal timescales off the Atlantic and Gulf coasts of the United States. Our results suggest that this finding also applies to intraseasonal timescales and to major river plumes around the world ocean. Piecuch et al. (2018) proposed a simplified theory to explain the causal relationship between river discharge and SSH variations. The theory essentially describes a steady-state balance between the two terms on the right-hand-side of Equation 1 but in terms of halosteric height, without considering mesoscale variability. In Section 3.3, we will discuss the relation between ΔQ and ΔSSH in relation to that theory.

3.2. Improvement of Model Skill

The results presented in Section 3.1 suggest that the inclusion of nonseasonal discharge has measurable impacts on model SSS and likely SSH as well near major river plumes. This motivates us to investigate whether the

Journal of Advances in Modeling Earth Systems

10.1029/2021MS002715

Table 3
Relationships Among ΔQ, ΔSSS, Its Temporal Tendency, and ΔSSH for Nonseasonal, Intraseasonal, and Interannual Time Scales at the Mouths of the World's Top Ten Rivers

			Amazon	Congo	Orinoco	Ganges-Brahmaputra	Changjiang	Parana	Yenisei	Lena	Mississippi	Mekong
#1	Mouth coordinates (longitude, latitude)		48.625°W, 1.125°N	12.125°E, 6.375°S	60.375°W, 9.125°N	90.625°E, 21.875°N	122.125°E, 31.125°N	56.125°W, 35.125°S	80.125°E, 73.375°N	129.875°E, 72.625°N	89.375°W, 28.875°N	106.625°E, 9.375°N
#2	Nonseasonal correlation	ΔQ, d(ΔSSS)/dt	−0.08	−0.10	−0.07	−0.11	−0.27	−0.27	−0.14	−0.27	−0.16	−0.20
#3		ΔQ, ΔSSS	−0.80	−0.83	−0.88	−0.49	−0.78	−0.82	−0.67	−0.33	−0.91	−0.76
#4		ΔSSS, ΔSSH	−0.96	−0.88	−0.85	−0.79	−0.94	−0.97	−0.90	−0.83	−0.95	−0.90
#5		ΔQ, ΔSSH	0.78	0.75	0.74	0.59	0.79	0.85	0.66	0.27	0.83	0.78
#6	Intraseasonal correlation	ΔQ, d (ΔSSS)/dt	−0.10	−0.14	−0.08	−0.12	−0.32	−0.34	−0.16	−0.28	−0.22	−0.25
#7		ΔQ, ΔSSS	−0.65	−0.78	−0.82	−0.31	−0.67	−0.71	−0.59	−0.14	−0.83	−0.64
#8		ΔSSS, ΔSSH	−0.99	−0.96	−0.98	−0.89	−0.97	−0.97	−0.95	−0.91	−0.96	−0.98
#9		ΔQ, ΔSSH	0.68	0.79	0.79	0.60	0.75	0.77	0.69	0.13	0.77	0.71
#10	Interannual-to-decadal correlation	ΔQ, d (ΔSSS)/dt	NS	NS	NS	NS	NS	NS	NS	−0.53	NS	NS
#11		ΔQ, ΔSSS	−0.93	−0.93	−0.94	−0.75	−0.93	−0.92	−0.92	−0.75	−0.97	−0.91
#12		ΔSSS, ΔSSH	−0.94	−0.83	−0.69	−0.57	−0.89	−0.96	−0.89	−0.83	−0.94	−0.80
#13		ΔQ, ΔSSH	0.83	0.73	0.66	0.48	0.85	0.91	0.80	0.58	0.88	0.86

Note. The coordinates of the river mouth locations are indicated in Row#1. The correlations between two variables are shown in rows 2–5 for nonseasonal time scales, in rows 6–9 for intraseasonal time scales, and in rows 10–13 for interannual-to-decadal time scales. All correlation coefficient values shown are statistically significant at the 95% confidence level. Insignificant correlation coefficients (not shown) are denoted by "NS".

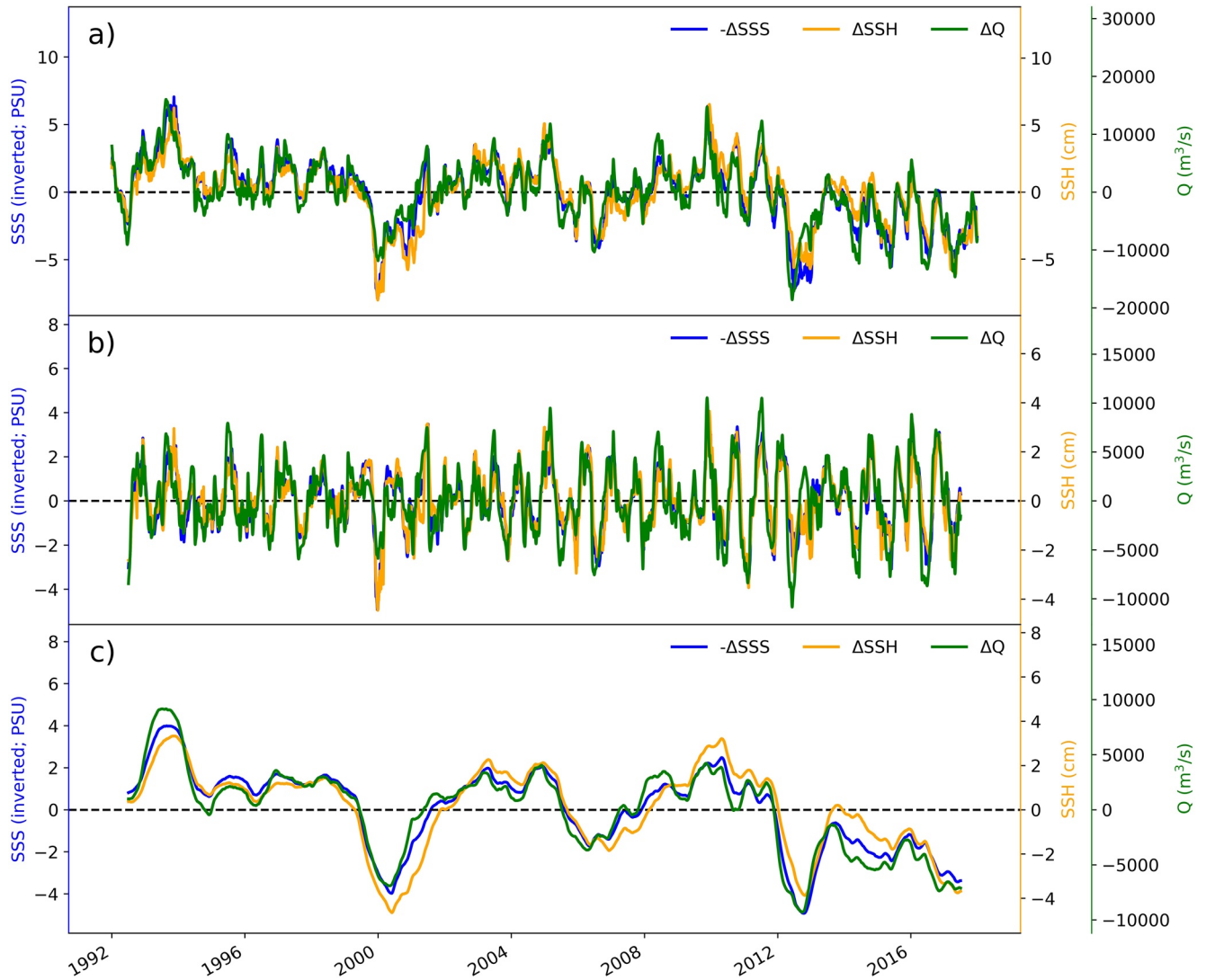

Figure 8. Time series of −ΔSSS and ΔSSH at a grid point near the Mississippi River mouth (see coordinates in Table 1 or 3) and Mississippi River discharge time series for (a) nonseasonal timescales, (b) intraseasonal timescales, (c) interannual-to-decadal timescales.

inclusion of nonseasonal discharge improves the model's representation of nonseasonal variations of SSS and SSH against observations.

We first compare the nonseasonal variations of model SSS from the *tot* and *clm* experiments with nonseasonal variations of SMOS SSS. Ideally, the comparison should be performed at the smoothing scales of the SMOS SSS product (approximately 70 km). However, such a comparison would implicitly include the comparison of mesoscale variability represented or misrepresented by the model and by SMOS. This is not preferable because (a) the relatively coarse resolution of the model that barely admits mesoscale variability, and (b) SMOS SSS are relatively noisy at this resolution. Moreover, the approximation of the coastlines and river mouth locations by the relatively coarse model could also result in errors in representing the exact locations of the river plumes. Because river plumes are associated with sharp spatial gradients in SSS, small differences in the position and shape of the model's river plume relative to observations can easily overwhelm the improvement in model SSS brought by the inclusion of nonseasonal discharge. These errors would exist even if the nonseasonal river discharge is perfectly accurate. In addition, the JRA55-do discharge data set, gridded at 25-km resolution, may also have errors in representing certain rivers.

Table 4
Statistics of Comparison Between SMOS SSS and SSS_{tot} (SSS_{clm}) Averaged Over 3° × 3° Boxes Near Major River Mouths in the Tropics and Subtropics for Nonseasonal, Intraseasonal, and Interannual Time Scales

		River	Amazon	Congo	Orinoco	Ganges-Brahmaputra	Changjiang	Parana	Mississippi	Mekong
#1	Box coordinates	longitude extent; latitude extent	48-51°W; 1-4°N	10-13°E; 6-9°S	58.5-61.5 °W; 8-11°N	89-92°E; 19-22°N	122-125°E; 30-33°N	54-57°W; 35-38°S	87-90°W; 27-30°N	106-109°E; 7.5-10.5°N
#2	Correlation	Nonseasonal	0.37 (0.24)	0.22 (0.35)	0.23 (0.12)	0.54 (0.47)	0.49 (0.28)	0.60 (0.56)	0.44 (-0.15)	0.25 (0.19)
		Intraseasonal	0.30 (0.24)	0.23 (0.43)	0.13 (NS)	0.24 (0.18)	0.31 (NS)	0.57 (0.49)	0.41 (0.14)	0.19 (0.24)
		Interannual-to-decadal	0.81 (NS)	NS (NS)	NS (NS)	0.90 (NS)	0.83 (NS)	NS (0.84)	0.86 (NS)	NS (NS)
#3	Variance explained (%)	Nonseasonal	10 (5)	NEG (NEG)	NEG (NEG)	26 (12)	13 (NEG)	35 (27)	6 (NEG)	NEG (NEG)
		Intraseasonal	8 (6)	NEG (7)	NEG (NEG)	NEG (NEG)	NEG (NEG)	32 (24)	1 (NEG)	NEG (NEG)
		Interannual-to-decadal	53 (13)	NEG (NEG)	NEG (1)	79 (50)	69 (45)	21 (43)	73 (NEG)	NEG (NEG)

Note. Linear trends are removed from the nonseasonal and interannual-to-decadal time series. The coordinates for the boxes are indicated in row#1. Correlation coefficients between SMOS SSS and SSS_{tot} (SSS_{clm}) are listed in row #2. The percentages of variance of SMOS SSS explained by SSS_{tot} (SSS_{clm}) are listed in row #3. All correlation coefficient values shown are statistically significant at the 95% confidence level. Insignificant correlation values (not shown) are denoted by "NS". Negative values for variance explained means no variance explained and are noted as "NEG". Value pairs in red indicate improvement due to the inclusion of nonseasonal discharge (i.e., SMOS SSS comparison with SSS_{tot} is better than that with SSS_{clm}). The values without paratheses are for the comparison between SMOS SSS and SSS_{tot}. Those within parentheses are for the comparison between SMOS SSS and SSS_{clm}.

To mitigate the model representation error and observational error (including that associated with mesoscale variability), we perform the model-observations comparison using averaged SSS over 3° × 3° grid boxes near the river mouths. The size of the box is selected to encompass the averaged spatial extent of enhanced SSS variability near major river plumes while suppressing mesoscale variability in the model and in SMOS SSS, thereby focusing the assessment of the impact of nonseasonal discharge on larger-scale SSS structure near river plumes. Using a slightly smaller or larger box does not change the conclusion presented below. Coastal SSS observations from SMOS within one satellite footprint (approximately 40 km from the coast) are subject to significant contamination by land signals because the sidelobes of the satellite antenna pattern encompass part of the land (Reul, Fournier, et al., 2014). These measurements are therefore excluded from the comparison. After excluding these land-contaminated SMOS SSS, the spatial averages within the 3° × 3° box are calculated over model grid points where both SMOS and model have SSS values.

In Table 4, we compare nonseasonal variations of SSS_{tot} and SSS_{clm} with the nonseasonal variations of SMOS SSS averaged over 3° × 3° boxes near the mouths of eight of the 10 largest rivers (row #1). The Lena and Yenisei rivers in the Arctic Ocean are excluded from the comparison because satellite SSS observations in high-latitude oceans are not reliable (e.g., Fournier et al., 2019). Row #2 and the associated sub-rows represent the correlation coefficients for nonseasonal, intraseasonal, and interannual variability between model and SMOS SSS, while row #3 and the associated sub-rows show the percentage variance of nonseasonal SMOS SSS explained by nonseasonal SSS_{tot} and SSS_{clm} for the three timescales. The values not enclosed by parentheses represent statistics for SMOS SSS versus SSS_{tot}, while the values within the parentheses show statistics for SMOS SSS versus SSS_{clm}. The values in red indicate that SSS_{tot} compares better with SMOS SSS than SSS_{clm} does. In other words, the values in red indicate that the inclusion of nonseasonal discharge forcing improves the model representation of nonseasonal SSS.

In general, we find statistically significant improvement in model SSS when nonseasonal discharge forcing is included. For nonseasonal time scales, for example, SSS_{tot} has better correlation with SMOS SSS than SSS_{clm} does for seven of the eight river-mouth regions (sub-row #1 of row #2 in Table 4) with the Congo River mouth being the only exception. The improvement near the Mississippi River mouth is particularly noteworthy, where the correlation between nonseasonal variations of SSS_{tot} and SMOS SSS (0.44) is much better than that between the nonseasonal variations of SSS_{clm} and SMOS SSS (−0.15). We also conducted similar analyses by separating the nonseasonal variations into intraseasonal and interannual-to-decadal time scales (sub-rows #2 and #3 in row #2). For the Amazon, Ganges-Brahmaputra, Changjiang, and Mississippi Rivers, the improvement due to the

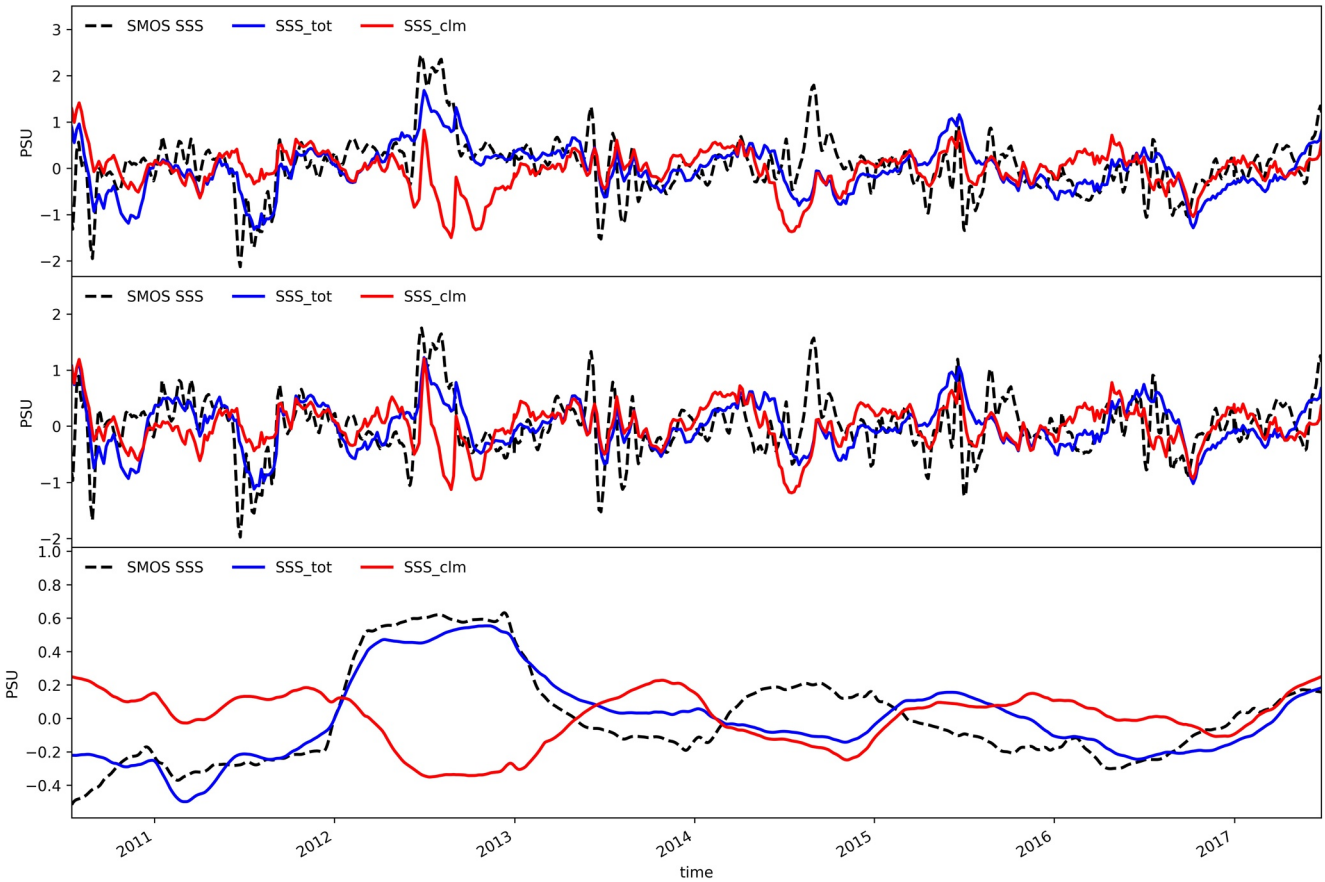

Figure 9. Comparison of SMOS SSS, SSS_{tot}, and SSS_{clm} averaged over a 3° × 3° box near the Mississippi River mouth for (a) nonseasonal, (b) intraseasonal, and (c) interannual timescales. Linear trends were removed from time series in (a) and (c).

inclusion of nonseasonal discharge is much more substantial on interannual-to-decadal than on intraseasonal timescales. For example, the correlation coefficients between the interannual-to-decadal variations of SSS_{tot} and SMOS SSS are 0.81, 0.90, 0.83, and 0.86 for the Amazon, Ganges-Brahmaputra, Changjiang, and Mississippi Rivers. In contrast, the correlation coefficients between the interannual-to-decadal variations of SSS_{clm} and SMOS SSS are smaller and not statistically significant. For the Orinoco and Parana Rivers, the improvement due to the inclusion of nonseasonal discharge occurs primarily on intraseasonal timescales, although the improvement is relatively minor. The improvement (or the lack of it) of the model SSS for a specific timescale is also likely related to the fidelity of the JRA55-do discharge variation on that timescale. An exception to these improvements is for the Congo River mouth region, where SSS_{tot} correlates worse with SMOS SSS than SSS_{clm} does. In fact, both SSS_{tot} and SSS_{clm} are poorly correlated with SMOS SSS. As discussed in more detail later in this section, this is likely related to the fidelity of the JRA55-do discharge.

We also compare the variance of SMOS SSS explained by SSS_{tot} and SSS_{clm} for nonseasonal, intraseasonal, and interannual timescales (row #3 and associated sub-rows in Table 4). For five of the eight rivers (Amazon, Ganges-Brahmaputra, Changjiang, Parana, and Mississippi), the variance of SMOS SSS explained by SSS_{tot} is generally larger than that explained by SSS_{clm}. Such improvement in explained variance is more obvious for interannual-to-decadal than for intraseasonal timescales except for the Parana River region. The most dramatic improvement in terms of explained variance is for the Mississippi River mouth on interannual timescales: with SSS_{tot} explaining 73% of the SMOS SSS variance on interannual timescales while SSS_{clm} does not explain any variance of SMOS SSS.

To illustrate the results related to Table 4 graphically, Figure 9 compares the SSS_{tot}, SSS_{clm}, and SMOS SSS time series for nonseasonal, intraseasonal, and interannual timescales using the Mississippi River mouth as an example. Figure 9a shows that the SSS_{tot} is overall closer to SMOS SSS than SSS_{clm} is. In particular, the negative

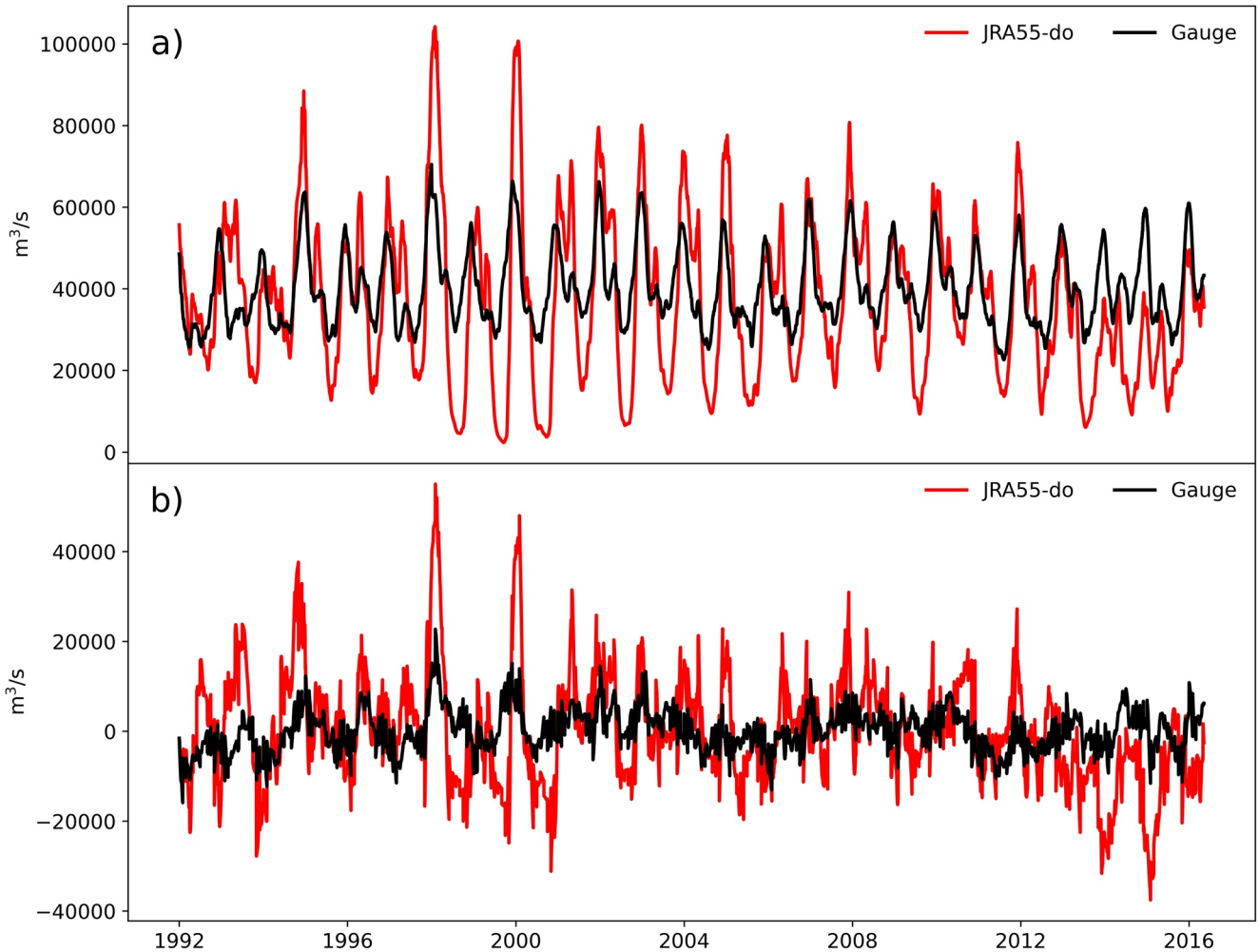

Figure 10. Comparison of total (a) and nonseasonal (b) discharge from JRA55-do and river gauge for the Congo River.

SMOS SSS anomalies in 2011 due to the Mississippi flooding in that year and positive SMOS SSS anomalies in 2012 due to the drought (Fournier, Lee, & Gierach, 2016) are captured by SSS_{tot} but not SSS_{clm}. In fact, SSS_{clm} shows erroneous negative SSS anomalies during the drought year of 2012. The comparison of intraseasonal variations for SMOS SSS, SSS_{tot}, SSS_{clm} (Figure 9b) shows that SSS_{tot} is not better than SSS_{clm} in terms of the overall difference from SMOS SSS, both poorly correlated with SMOS SSS. However, for specific events such as the 2011 Mississippi flood and the 2012 drought events, the intraseasonal SSS_{tot} is more consistent with SMOS SSS than the intraseasonal SSS_{clm} is.

The level of improvement of model SSS relative to SMOS SSS due to the inclusion of nonseasonal discharge depends on the fidelities of the (a) JRA55-do discharge, (b) SMOS SSS, and (c) model physics for various timescales. Extensive investigations are needed to examine which of these three factors (or their combinations) is responsible for the lack of improvement for certain rivers on certain timescales. Because the lack of improvement of model SSS is the most conspicuous for the Congo River mouth, we conducted some analyses for this river mouth and presented the results below.

We first assess the fidelity of Congo River discharge estimates from JRA55-do. Figure 10 compares the times series of total and nonseasonal discharge between JRA55-do and river gauge data at Brazzaville near Kinshasa (at 15.3°E and 4.3°S), managed by SO-HYBAM Amazon basin water resources observation service, (https://hybam.obs-mip.fr/). Large discrepancies are seen between the JRA55-do estimates and river gauge data. This is not surprising from a hydrological perspective. The Congo Basin has complex hydrology due to bi-modal rainfall distribution caused by the seasonal shift of the Intertropical Convergence Zone and a thick rainforest whose

Table 5
Same as Table 4, but for SSH From the Model and SSH Observations From Merged Altimetry

		River	Amazon	Congo	Orinoco	Ganges-Brahmaputra	Changjiang	Parana	Mississippi	Mekong
#1	Box coordinates	longitude extent; latitude extent	48-51°W; 1-4°N	10-13°E; 6-9°S	58.5-61.5 °W; 8-11°N	89-92°E; 19-22°N	122-125°E; 30-33°N	54-57°W; 35-38°S	87-90°W; 27-30°N	106-109°E; 7.5-10.5°N
#2	Correlation	Nonseasonal	0.23 (0.13)	0.69 (0.71)	0.40 (0.40)	0.77 (0.78)	0.38 (0.37)	0.18 (0.16)	0.37 (0.40)	0.31 (0.30)
		Intraseasonal	0.09 (0.08)	0.67 (0.67)	0.26 (0.26)	0.58 (0.58)	0.28 (0.28)	0.14 (0.13)	0.24 (0.24)	0.23 (0.23)
		Interannual-to-decadal	0.46 (NS)	0.70 (0.80)	0.69 (0.63)	0.91 (0.88)	0.68 (0.64)	0.57 (0.60)	0.44 (0.52)	0.60 (0.53)
#3	Variance explained (%)	Nonseasonal	NEG (NEG)	5 (19)	1 (NEG)	58 (56)	NEG (NEG)	NEG (NEG)	11 (14)	NEG (NEG)
		Intraseasonal	NEG (NEG)	NEG (NEG)	NEG (NEG)	15 (15)	NEG (NEG)	NEG (NEG)	3 (3)	NEG (NEG)
		Interannual-to-decadal	14 (NEG)	23 (53)	44 (38)	82 (78)	28 (25)	32 (34)	11 (23)	19 (9)

Note. The significance of the red color in Table 5 is the same as that in Table 4, except that in Table 5 the red color indicates improvement of model SSH with respect to SSH observations.

interaction with hydrology is far less understood than that for the Amazon rainforest (Hua et al., 2019; Washington et al., 2013). Furthermore, the lack of field observations of climate variables from the Congo River region due to geopolitical reasons has hampered the representation of physical processes in land-surface and atmospheric models for this region (Hua et al., 2019). JRA55-do is based on the JRA55 atmospheric reanalysis. The latter, like other reanalyses, is likely subject to these limitations over the Congo River basin.

Next, we discuss the fidelity of SMOS SSS near the Congo River mouth. Fournier and Lee (2021) found that the variations of SMOS SSS averaged within 3° × 3° of this river mouth have excellent consistency with those from the SMAP satellite, with a correlation coefficient of nearly 1.0 and standard deviation difference between the two satellite SSS products being approximately 0.3 psu. The study also reported that satellite SSS is significantly correlated with two in-situ gridded SSS products (0.86 between SMOS and in-situ products, and 0.90 between SMAP and in-situ products). The in-situ gridded SSS agree well with satellite SSS in magnitude after the low-discharge season but have much smaller magnitudes of freshening after the high-discharge season, attributable to the under-sampling of the spatiotemporal variability of the river plume by the sparsely distributed in-situ measurements during the latter season. Moreover, the discrepancy between the two in-situ products (approximately 0.4 psu) is somewhat larger than that between SMOS and SMAP (0.3 psu).

Based on the results described in the two paragraphs above, we conclude that the lack of improvement of model SSS with respect to SMOS SSS when nonseasonal discharge was included is primarily related to the fidelity of Congo River discharge estimate from JRA55-do, rather than to the error of SMOS SSS. Model error due to physics may also contribute. Future investigations are needed to study what aspect of the model limitations may hinder the improvement of model SSS at this river mouth.

In addition to SSS, we also compare model SSH with altimeter-derived gridded SSH averaged over 3° × 3° of the river mouths (Table 5). The improvement in model SSH relative to the altimetric SSH with the inclusion of nonseasonal discharge is much less notable compared to the improvement of model SSS shown in Table 4. Moreover, the improvement in model SSH occurs primarily on interannual-to-decadal time scales for five of the eight rivers (Amazon, Orinoco, Ganges-Brahmaputra, Changjiang, and Mekong) both in terms of correlation and variance explained (the last sub-row of rows #2 and #3). Except for the Amazon River region, the improvement is quite minor. As discussed in Section 3.1 in relation to of $R_\sigma(SSS)$ (Figure 6) and of $R_\sigma(SSH)$ (Figure 7), nonseasonal SSH is much more dominated by the effect of atmospheric forcing than by the effect of river discharge comparing to the case for nonseasonal SSS. That makes it more difficult to improve nonseasonal SSH, especially since the atmospheric forcing contains errors. In fact, for many boxes near the major river mouths, the temporal variations of SSH from the *tot* and *clm* experiments both compare poorly with the gridded altimeter product,

likely contributed to the error in wind forcing. Such an error can cause unrealistic model SSH in response to local winds or fast coastally trapped waves induced by remote winds. Moreover, different representations of instability between the model and observation can also degrade the comparison. Nevertheless, the lack of improvement of model SSH over the 3° × 3° boxes relative to the altimetric SSH data does not necessarily mean that nonseasonal river discharge has no impact on coastal SSH. In addition to 3° × 3° boxes, we also compared model SSH for the grid point at the river mouth with altimetric SSH. We could not identify any significant improvement because of two reasons. First, mesoscale variability at one grid point can overwhelm the potential improvement of SSH due to the inclusion of nonseasonal discharge, especially given the significant error of the model in representing mesoscale variability because of the limited resolution. Second, coastal altimetry data are known to have larger uncertainties.

Given the issues with the comparison with altimetry SSH, we compared the model simulations with tide gauge data. Coastal tide gauge data are usually not located right at the river mouths. While data are available near some of the major river mouths, most of them are not up-to-date. Near the Mississippi River mouth, tide gauge data are available at Grand Isle (Station # 526 from Permanent Service for Mean Sea Level, PSMSL). Figure 11 provides a comparison of these tide gauge observations with SSH_{tot} and $SSH_{clm.}$The correlations of SSH_{tot} and SSH_{clm} with tide gauge data for nonseasonal timescales (Figure 11a) are both about 0.7, with the model SSH explaining 44% of the observed SSH variance for nonseasonal timescales. The comparison is similar for intraseasonal timescales (Figure 11b). For interannual timescales (Figure 11c), SSH_{tot} correlates with the tide gauge data slightly better than SSH_{clm} (with a correlation coefficient of 0.8 vs. 0.7). SSH_{tot} also explains more variance of the tide gauge data than SSH_{clm} for interannual timescales (63% vs. 53%). The improvement is particularly obvious during the 2000–2001 period when both SSH_{tot} and the observed SSH show negative anomalies up to 6 cm. This anomaly is consistent with the large decrease in Mississippi River discharge, as seen in Figure 8c. SSH_{clm} failed to capture this anomaly. Note that the tide gauge data can be affected by small-scale (e.g., mesoscale and submesoscale) variability that the model cannot represent, which could affect the comparison between model and tide gauge SSH for certain periods.

The results presented in this section suggest that the inclusion of nonseasonal discharge results in notable improvement of the model representations of SSS with respect to satellite SSS near several major river mouths and of SSH against tide gauge data downstream of the Mississippi River mouth. The results also provide further support that nonseasonal discharge ΔQ is an important factor influencing the difference in nonseasonal SSS and SSH between the two runs, namely, ΔSSS and ΔSSH.

3.3. Mechanistic Explanation of Discharge Influence on Sea Surface Height

In Section 3.1, we show that there are strong correlations among ΔQ, ΔSSS, and ΔSSH near major river mouths. In this section, we provide a theoretical explanation of how nonseasonal discharge can influence ΔSSH. We estimate ΔSSH through two methods: (a) by estimating the effect of salinity difference between the two experiments on halosteric height; and (b) using the simplified theory proposed by Piecuch et al. (2018) to estimate ΔSSH using nonseasonal discharge.

In the first method, we use ΔSSS to estimate ΔSSH because both of them are associated with nonseasonal discharge. Near river mouths, salinity changes due to discharge are usually heavily confined to the upper layer, H_0. From the inflection depth of the vertical profiles of model salinity at the Mississippi River mouth, we determined H_0 to be approximately 10 m. We assume ΔSSS to be representative of the average salinity anomaly in this upper layer. The halosteric height difference between the two experiments, ΔSSH_{es}, can then be estimated by (following Lee et al., 2019):

$$\Delta SSH_{es} = -\beta H_0 \Delta SSS_{H_0} \tag{2}$$

where ΔSSS_{H_0} is representative of salinity changes in the upper layer H_0, and β is the saline contraction coefficient, taken to be $\beta = 7.6 \times 10^{-4}\ psu^{-1}$ (Lee et al., 2019).

The second method used the analytical theory developed by Piecuch et al. (2018) based on conservation of volume, salt, and offshore momentum in the far-field of a coastal river plume. The theory is used to evaluate ΔSSH directly from ΔQ by estimating the halosteric changes caused by ΔQ, affected by the entrainment of ambient salinity as the ocean currents carry the riverine freshwaters downstream. Based on this theory, we computed the

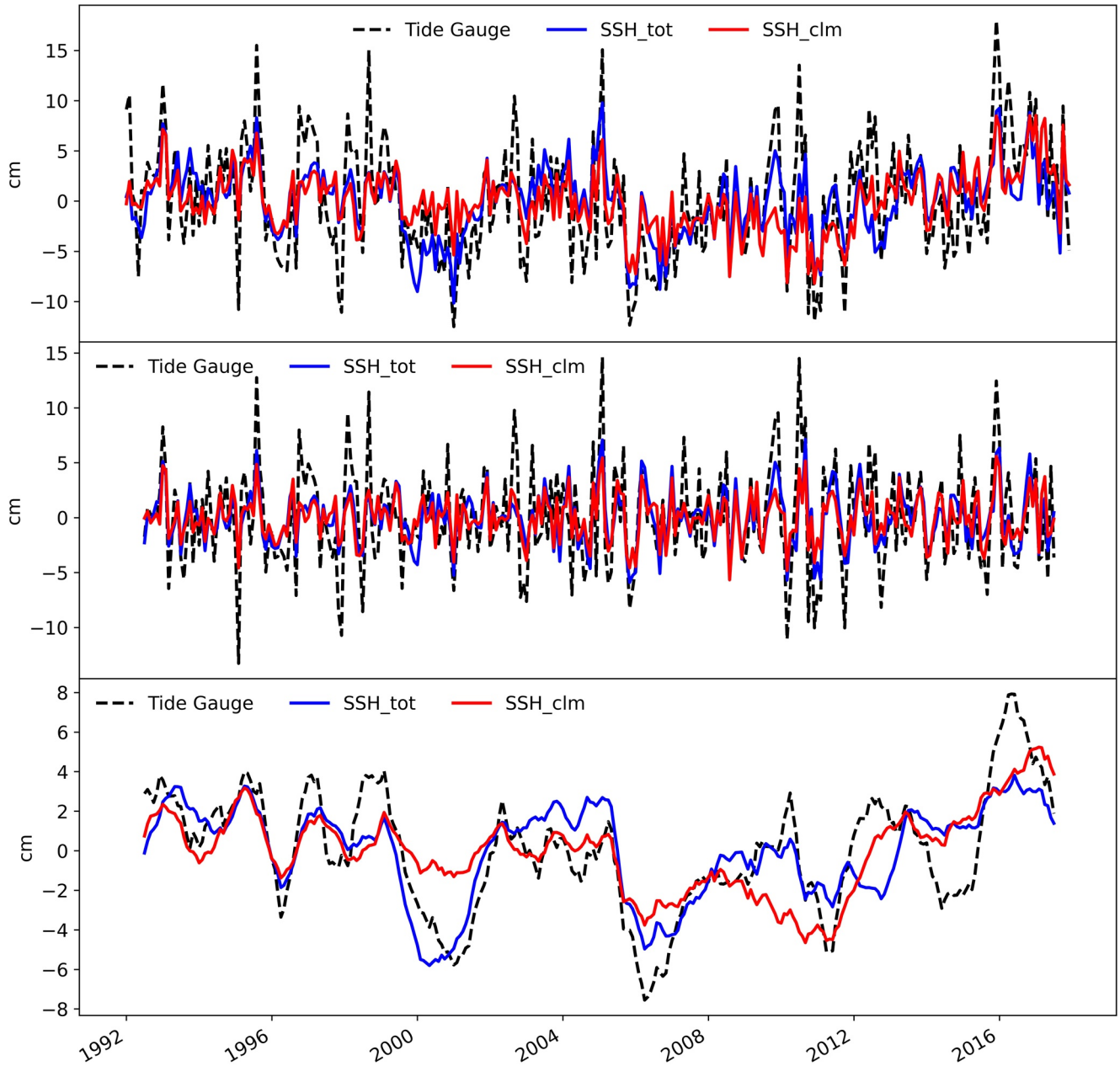

Figure 11. Comparison of nonseasonal SSH_{tot} and SSH_{clm} with nonseasonal SSH observed by tide gauge data from the Grand Isle near the Mississippi River mouth for (a) nonseasonal, (b) intraseasonal, and (c) interannual timescales. Linear trends were removed from time series in (a) and (c).

theoretical estimates of nonseasonal SSH differences between the two experiments (ΔSSH_{er}) using the following equation adapted from Piecuch et al. (2018),

$$\Delta SSH_{er} = \text{sqrt}\left(\frac{f\beta S_0}{2gQ_F}\right)\Delta Q_F \tag{3}$$

where f is the Coriolis parameter, β is the saline compression coefficient as described earlier, S_0 is the entrainment or ambient salinity (assumed to be 35 psu), g is the gravitational acceleration, Q_F is the river discharge, and ΔQ_F is the nonseasonal discharge. Because of the dependence on f, the theory is not valid near the equator.

Figure 12 compares ΔSSH_{es} estimated from Equation 2 and ΔSSH_{er} estimated from Equation 3 with the actual ΔSSH obtained from the model experiments for a grid point at the Mississippi River mouth for nonseasonal,

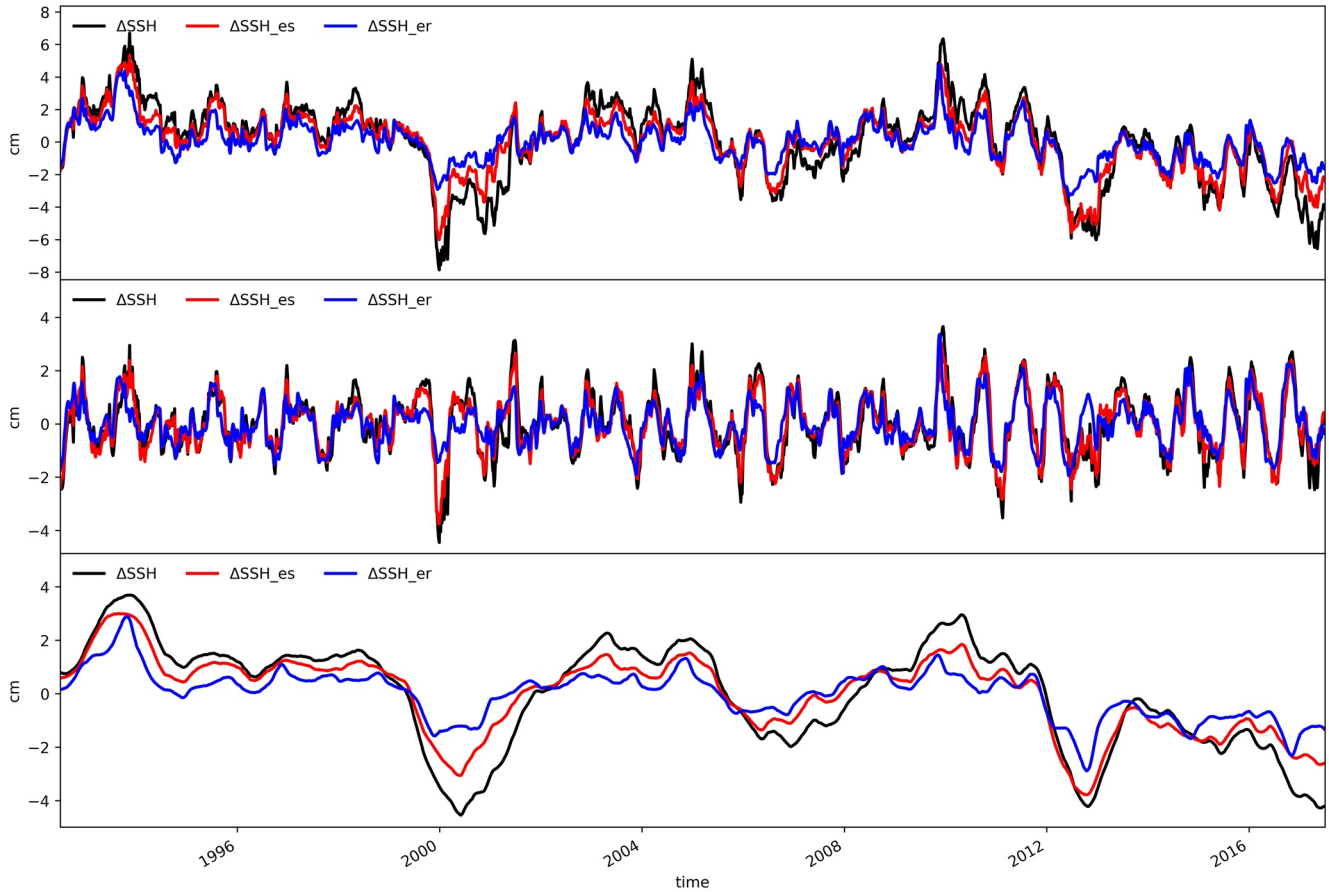

Figure 12. Comparison of ΔSSH at the Mississippi River mouth simulated by the model with that estimated using the ΔSSS-based method (ΔSSH_es) and that using nonseasonal discharge and the simple theory of Piecuch et al. (2018) (ΔSSH_er) for (a) nonseasonal, (b) intraseasonal, and (c) interannual-to-decadal timescales.

intraseasonal, and interannual-to-decadal timescales in the three different panels. Both ΔSSH_{es} and ΔSSH_{er} provide a reasonable estimate of ΔSSH. However, the SSS-based estimation (ΔSSH_{es}) provides a more accurate estimate of ΔSSH than the discharge-based estimation (ΔSSH_{er}) in terms of temporal coherence as well as amplitude. In particular, ΔSSH_{er} generally underestimates the amplitude of the ΔSSH variation. This is consistent with the finding reported by Piecuch et al. (2018) where the predicted SSH variability for US East and Gulf coasts on interannual-to-decadal timescales was also found to be underestimated. The correlation coefficient between ΔSSH_{es} and ΔSSH ranges from 0.96 to 0.97 depending on time scales, with ΔSSH_{es} explaining approximately 87%–91% of the variance of ΔSSH. In contrast, the correlation coefficient between ΔSSH_{er} and ΔSSH ranges from 0.78 to 0.89, with ΔSSH_{er} explaining only about 59%–60% of the variance of ΔSSH.

We also performed such a comparison at the grid locations of the river mouths for the world's 10 largest rivers. The statistics of the comparison are summarized in Table 6, with row #2 showing the correlation coefficients between ΔSSH simulated by the model and the estimated ΔSSH from the two methods (ΔSSH_{es} and ΔSSH_{er}). Row #3 shows the percentage variance of ΔSSH explained by ΔSSH_{es} and ΔSSH_{er}. The sub-rows within each row provide the statistics for nonseasonal, intraseasonal, and interannual-to-decadal timescales. The statistics for ΔSSH_{es} versus ΔSSH are shown without parentheses while those for ΔSSH_{er} versus ΔSSH are enclosed by parentheses.

The statistics provided in Table 6 suggest that the SSS-based estimation method is consistently more skillful in estimating ΔSSH than the discharge-based estimation method across these major river mouths for all timescales presented. The difference in skill between the two methods is particularly large for the Amazon, Yenisei, and Lena rivers, especially in terms of explained variance. For the Amazon River, the SSS-based method explains approximately 95% of the variance of ΔSSH whereas the discharge-based method only explains approximately 30% of the variance of ΔSSH. This is related to the limitation of applying the theory developed by Piecuch

Table 6
Comparison Among ΔSSH Simulated by the Model Experiments and the Estimated ΔSSH Using the SSS-Based Method (ΔSSH_{es}) and That Using the Discharge-Based Method (ΔSSH_{er}) for World's Ten Largest Rivers

	River	Amazon	Congo	Orinoco	Ganges-Brahmaputra	Changjiang	Parana	Yenisei	Lena	Mississippi	Mekong
#1	Mouth coordinates (longitude, latitude)	48.625°W, 1.125°N	12.125°E, 6.375°S	60.375°W, 9.125°N	90.625°E, 21.875°N	122.125°E, 31.125°N	56.125°W, 35.125°S	80.125°E, 73.375°N	129.875°E, 72.625°N	89.375°W, 28.875°N	106.625°E, 9.375°N
#2	Correlation										
	Nonseasonal	0.97 (0.83)	0.89 (0.78)	0.90 (0.79)	0.85 (0.67)	0.96 (0.81)	0.98 (0.85)	0.93 (0.64)	0.86 (0.28)	0.96 (0.85)	0.94 (0.83)
	Intraseasonal	0.99 (0.71)	0.96 (0.79)	0.98 (0.83)	0.89 (0.55)	0.97 (0.74)	0.97 (0.77)	0.95 (0.66)	0.91 (0.09)	0.96 (0.78)	0.98 (0.72)
	Interannual-to-decadal	0.97 (0.83)	0.88 (0.79)	0.77 (0.64)	0.75 (0.62)	0.94 (0.88)	0.98 (0.91)	0.94 (0.70)	0.85 (0.46)	0.97 (0.89)	0.91 (0.83)
#3	Variance explained (%)										
	Nonseasonal	94 (32)	78 (51)	79 (53)	65 (40)	90 (65)	94 (68)	76 (36)	72 (NEG)	88 (60)	62 (49)
	Intraseasonal	96 (27)	87 (60)	96 (56)	67 (0)	90 (48)	93 (58)	86 (2)	82 (NEG)	91 (59)	57 (47)
	Interannual-to-decadal	92 (31)	73 (41)	57 (38)	53 (16)	99 (74)	93 (70)	67 (48)	70 (NEG)	87 (60)	65 (57)

Note. Row #1 indicates river mouth coordinates (Same as Tables 1 and 2). Row #2 shows the correlation coefficients between ΔSSH and ΔSSH_{es} without parantheses and between ΔSSH and ΔSSH_{er} (enclosed by parentheses). Sub-rows show the analysis for nonseasonal, intraseasonal, and interannual-to-decadal timescales. Row #3 shows a similar comparison, but for percentage variance of ΔSSH explained by ΔSSH_{es} (without parentheses) and by ΔSSH_{er} (enclosed by parentheses).

et al. (2018) to a river plume near the equator because the theory depends on the Coriolis parameter *f*. For the Lena River, the SSS-based method explains 72%–82% of the variance of ΔSSH, whereas the discharge-based method does not explain any variance of ΔSSH. The reason for the poor skill of the discharge-based theory to predict ΔSSH for the Arctic river needs further investigation.

Note that the SSS-based method is a kinematic approach based on the halosteric height effect, whereas the simple theory of Piecuch et al. (2018) provides dynamical interpretation. However, the comparison of the predicted SSH variability between the two methods and the model simulations in this study provides a basis for future effort to improve the discharge-based method to estimate coastal SSH changes using discharge information, for example, by revisiting the assumptions used in developing the simple theory of Piecuch et al. (2018). Piecuch et al. (2018) discussed several such aspects that can potentially improve the performance of the theory.

4. Conclusion

Nonseasonal discharge is found to have measurable impacts on SSS and SSH near major river plumes. The standard deviations of nonseasonal SSS (SSH) caused by nonseasonal discharge at the mouths of the 10 largest rivers range from 1.3 to 3 psu (1–2.7 cm). Certain events associated with intraseasonal and interannual-to-decadal discharge variations can induce much larger changes in SSS and SSH. SSH changes caused by nonseasonal discharge can be explained by the salinity effect on halosteric height and can be inferred accurately from the associated SSS changes. We also assess the skill of the simple theory proposed by Piecuch et al. (2018) using river discharge to infer the impacts on SSH. We find that the theory is able to predict the impacts on SSH at intraseasonal and interannual-to-decadal timescales reasonably well in terms of temporal correlation. However, the theory underestimates the amplitude of the SSH changes for the top 10 rivers on intraseasonal to interannual-to-decadal timescales, consistent with results from Piecuch et al. (2018) study on the US east and Gulf coasts at interannual-to-decadal timescales. Our evaluation of this theory goes beyond the scope of the study by Piecuch et al. (2018) by including the analysis for major rivers around the world ocean and by including the intraseasonal timescales. We also find that the theory has a more limited skill when being applied to river plumes near the equator (where the Coriolis parameter is small) and in the Arctic Ocean. Our model experiments can be used as a testbed for improving the theory in future studies, for example, by revisiting the assumptions.

The inclusion of nonseasonal discharge improved model simulation of nonseasonal SSS in comparison to satellite SSS observations within a few degrees of seven of the eight major river mouths in the tropics and midlatitudes (the only exception being the Congo River mouth). The improvement of model SSS is generally more notable for interannual-to-decadal than for intraseasonal timescales. Nonseasonal discharge also leads to some improvement of model SSH against satellite SSH within a few degrees of five of the eight major river mouths in the tropics and midlatitudes on interannual-to-decadal time scales. The SSH improvement is minor except near the Amazon River mouth against satellite SSH and near the Mississippi River mouth against tide-gauge SSH.

The relatively large SSS changes at river mouths due to the inclusion of nonseasonal discharge have strong implications for marine biology, ecosystem, and biogeochemistry. For example, such changes in SSS need to be accounted for in modeling studies of total alkalinity that is linearly correlated with salinity (Lee et al., 2006) as well as ocean acidification and air-sea CO_2 flux that depend on total alkalinity.

Our findings underscore the importance of including nonseasonal discharge in global ocean models to facilitate interdisciplinary research and coastal sea level investigations.

There are a number of directions worth exploring beyond this study by investigating the potential impacts of model limitations on the response to nonseasonal discharge and the impacts of nonseasonal discharge on other aspects of the model ocean. The ocean model used in this study has 12–30 km horizontal grid spacing. While such resolutions are typical of global ocean data-assimilative and climate models, they are insufficient to simulate the smaller-scale salinity structure along the coasts associated with river plumes such as those discussed by Holt et al. (2017). Feng et al. (2021) has conducted a preliminary assessment of the impact of JRA55-do discharge in various ECCO solutions of different resolutions, including LLC270. The use of higher-resolution models would be of interest to further investigate the impacts of nonseasonal discharge on SSS and SSH near the river mouths. Given the computational cost, targeted regional high-resolution models would be an amenable approach. Moreover, adopting an estuary box model such as that implemented into the Community Earth System Model can also improve the representation of the effect of riverine water in global ocean models (Danabasoglu et al., 2020; Sun et al., 2017, 2019). The sensitivity of the model to mixing formulations near river mouths, which is important for riverine water dispersal (e.g., Benshila et al., 2014), and the impact of tides are also of interest for future investigation. The current study only focused on SSS and SSH. Future extension of the study is worthwhile by investigating the effects of nonseasonal discharge on additional oceanic properties such as near-surface stratification as well as the depths of the mixed layer and the barrier layer.

Data Availability Statement

The JRA55-do discharge data set is available through https://esgf-node.llnl.gov/search/input4mips/. The SMOS SSS product used is obtained from https://www.catds.fr/Products/Available-products-from-CEC-OS/CEC-Locean-L3-Debiased-v4. The SMAP SSS product used is obtained from https://podaac.jpl.nasa.gov/dataset/SMAP_JPL_L3_SSS_CAP_8DAY-RUNNINGMEAN_V4. The gridded SSH product is obtained from https://resources.marine.copernicus.eu/?option=com_csw&task=results?option=com_csw&view=details&product_id=SEALEVEL_GLO_PHY_L4_REP_OBSERVATIONS_008_047. Congo River gauge discharge data is obtained from https://hybam.obs-mip.fr/. The 5-day averaged sea surface height and sea surface salinity outputs from the model simulation using climatological river discharge are available through https://doi.org/10.5281/zenodo.5102918 and https://doi.org/10.5281/zenodo.5104411, respectively. The 5-day averaged sea surface height and sea surface salinity outputs from the model simulation using daily river discharge are available through https://doi.org/10.5281/zenodo.5102918 and https://doi.org/10.5281/zenodo.5104411, respectively. These files are in Matlab mat file format and can be read using Matlab's load command. These files are also available through (https://ecco.jpl.nasa.gov/drive/files/ECCO2/LLC270/Influence_of_Nonseasonal_River_Discharge), together with a readme file accessible by users who have registered an account in (https://earthdata.nasa.gov/).

Acknowledgments
This research was carried out in part at the Jet Propulsion Laboratory, California Institute of Technology, under a contract with the National Aeronautics and Space Administration (80NM0018D0004) with support from the Physical Oceanography (PO) and Modeling, Analysis, and Prediction (MAP) Programs. High-end computing resources for the numerical simulation were provided by the NASA Advanced Supercomputing Division at the Ames Research Center. We sincerely thank the reviewers for their helpful comments and patient input that led to improvements of the manuscript.

References

Akhil, V. P., Lengaigne, M., Vialard, J., Durand, F., Keerthi, M. G., Chaitanya, A. V. S., et al. (2016). A modeling study of processes controlling the Bay of Bengal sea surface salinity interannual variability. *Journal of Geophysical Research: Oceans*, *121*, 8471–8495. https://doi.org/10.1002/2016JC011662

Balaguru, K., Chang, P., Saravanan, R., & Jang, C. J. (2012). The barrier layer of the Atlantic warm pool: Formation mechanism and influence on the mean climate. *Tellus, Series A: Dynamic Meteorology and Oceanography*, *64*(1), 18162. https://doi.org/10.3402/tellusa.v64i0.18162

Ballarotta, M., Ubelmann, C., Pujol, M.-I., Taburet, G., Fournier, F., Legeais, J.-F., et al. (2019). On the resolutions of ocean altimetry maps. *Ocean Science*, *15*, 1091–1109. https://doi.org/10.5194/os-15-1091-2019

Benshila, R., Durand, F., Masson, S., Bourdallé-Badie, R., de Boyer Montégut, C., Papa, F., & Madec, G. (2014). The upper Bay of Bengal salinity structure in a high-resolution model. *Ocean Modelling*, *74*, 36–52. https://doi.org/10.1016/j.ocemod.2013.12.001

Boano, F., Harvey, J. W., Marion, A., Packman, A. I., Revelli, R., Ridolfi, L., & Wörman, A. (2014). Hyporheic flow and transport processes: Mechanisms, models, and biogeochemical implications. *Reviews of Geophysics*, *52*, 603–679. https://doi.org/10.1002/2012RG000417

Boutin, J., Chao, Y., Asher, W. E., Delcroix, T., Drucker, R., Drushka, K., et al. (2016). Satellite and in situ salinity: Understanding near surface stratification and sub-footprint variability. *Bulletin of the American Meteorological Society*, *97*(Issue 8), 1391–1407. https://doi.org/10.1175/BAMS-D-15-00032.1

Boutin, J., Vergely, J. L., Marchand, S., D'Amico, F., Hasson, A., Kolodziejczyk, N., et al. (2018). New SMOS Sea Surface Salinity with reduced systematic errors and improved variability. *Remote Sensing of Environment*, *214*, 115–134. https://doi.org/10.1016/j.rse.2018.05.022

Chandanpurkar, H. A., Reager, J. T., Famiglietti, J. S., & Syed, T. H. (2017). Satellite- and reanalysis-based mass balance estimates of global continental discharge (1993–2015). *Journal of Climate*, *30*(21), 8481–8495. https://doi.org/10.1175/JCLI-D-16-0708.1

Chao, Y., Farrara, J. D., Schumann, G., Andreadis, K. M., & Moller, D. (2015). Sea surface salinity variability in response to the Congo river discharge. *Continental Shelf Research*, *99*, 35–45. https://doi.org/10.1016/j.csr.2015.03.005

Dai, A., Qian, T., Trenberth, K. E., & Milliman, J. D. (2009). Changes in continental freshwater discharge from 1948 to 2004. *Journal of Climate*, *22*(10), 2773–2792. https://doi.org/10.1175/2008JCLI2592.1

Danabasoglu, G., Lamarque, J. F., Bachmeister, J., Bailey, D. A., DuVivier, A. K., Edwards, J., et al. (2020). The Community Earth System Model Version 2 (CESM2). *Journal of Advances in Modeling Earth Systems*, *12*, e01916. https://doi.org/10.1029/2019MS001916

Dandapat, S., Gnanaseelan, C., & Parekh, A. (2020). Impact of excess and deficit river runoff on Bay of Bengal upper ocean characteristics using an ocean general circulation model. *Deep Sea Research Part II: Topical Studies in Oceanography*, *172*, 104714. ISSN 0967-0645. https://doi.org/10.1016/j.dsr2.2019.104714

Dieng, H. B., Dadou, I., Léger, F., Morel, Y., Jouanno, J., Lyard, F., & Allain, D. (2019). Sea level anomalies using altimetry, model and tide gauges along the African coasts in the Eastern Tropical Atlantic Ocean: Inter-comparison and temporal variability. *Advances in Space Research*, *68*(2), 534–552. ISSN 0273-1177. https://doi.org/10.1016/j.asr.2019.10.019

Durand, F., Papa, F., Rahaman, A., & Bala, S. K. (2011). Impact of Ganges–Brahmaputra interannual discharge variations on Bay of Bengal salinity and temperature during 1992–1999 period. *Journal of Earth System Science*, *120*, 859–872. https://doi.org/10.1007/s12040-011-0118-x

Durand, F., Piecuch, C. G., Becker, M., Papa, F., Raju, S. V., Khan, J. U., & Ponte, R. M. (2019). Impact of continental freshwater runoff on coastal sea level. *Surveys in Geophysics*, *40*, 1437–1466. https://doi.org/10.1007/s10712-019-09536-w

Fekete, B. M., Vörösmarty, C. J., & Grabs, W. (2002). High-resolution fields of global runoff combining observed river discharge and simulated water balances. *Global Biogeochemical Cycles*, *16*(3), 15-1-15–10. https://doi.org/10.1029/1999gb001254

Feng, Y., Menemenlis, D., Xue, H., Zhang, H., Carroll, D., Du, Y., & Wu, H. (2021). Improved representation of river runoff in Estimating the Circulation and Climate of the Ocean Version 4 (ECCOv4) simulations: Implementation, evaluation, and impacts to coastal plume regions. *Geoscientific Model Development*, *14*(3), 1801–1819. https://doi.org/10.5194/gmd-14-1801-2021

Fore, A. G., Yueh, S. H., Tang, W., Stiles, B. W., & Hayashi, A. K. (2016). Combined active/passive retrievals of ocean vector wind and sea surface salinity with SMAP. *IEEE Transactions on Geoscience and Remote Sensing*, *54*(12), 7396–7404. https://doi.org/10.1109/tgrs.2016.2601486

Forget, G., Campin, J.-M., Heimbach, P., Hill, C. N., Ponte, R. M., & Wunsch, C. (2015). ECCO version 4: An integrated framework for non-linear inverse modeling and global ocean state estimation. *Geoscientific Model Development Discussions*, *8*(5), 3653–3743. https://doi.org/10.5194/gmdd-8-3653-2015

Fournier, S., & Lee, T. (2021). Seasonal and interannual variability of sea surface salinity near major river mouths of the world ocean inferred from gridded satellite and in-situ salinity products. *Remote Sensing*, *13*, 728. https://doi.org/10.3390/rs13040728

Fournier, S., Lee, T., & Gierach, M. M. (2016). Seasonal and interannual variations of sea surface salinity associated with the Mississippi River plume observed by SMOS and Aquarius. *Remote Sensing of Environment*, *180*, 431–439. https://doi.org/10.1016/j.rse.2016.02.050

Fournier, S., Lee, T., Tang, W., Steele, M., & Olmedo, E. (2019). Evaluation and intercomparison of SMOS, Aquarius, and SMAP sea surface salinity products in the Arctic Ocean. *Remote Sensing*, *11*(24), 3043. https://doi.org/10.3390/rs11243043

Fournier, S., Reager, J. T., Lee, T., Vazquez-Cuervo, J., David, C. H., & Gierach, M. M. (2016). SMAP observes flooding from land to sea: The Texas event of 2015. *Geophysical Research Letters*, *43*(19), 10338–10346. https://doi.org/10.1002/2016GL070821

Fournier, S., Vialard, J., Lengaigne, M., Lee, T., Gierach, M. M., & Chaitanya, A. V. S. (2017). Modulation of the Ganges-Brahmaputra river plume by the Indian Ocean Dipole and eddies inferred from satellite observations. *Journal of Geophysical Research: Oceans*, *122*(12), 9591–9604. https://doi.org/10.1002/2017JC013333

Garvine, R. W. (1995). A dynamical system for classifying buoyant coastal discharges. *Continental Shelf Research*, *15*(13), 1585–1596. https://doi.org/10.1016/0278-4343(94)00065-U

Gaspar, P., Grégoris, Y., & Lefevre, J.-M. (1990). A simple eddy kinetic energy model for simulations of the oceanic vertical mixing: Tests at station Papa and long-term upper ocean study site. *Journal of Geophysical Research*, *95*(C9), 16179. https://doi.org/10.1029/jc095ic09p16179

Gent, P. R., & Mcwilliams, J. C. (1990). Isopycnal mixing in ocean circulation models. *Journal of Physical Oceanography*, *20*(1), 150–155. https://doi.org/10.1175/1520-0485(1990)020<0150:imiocm>2.0.co;2

Gierach, M. M., Vazquez-Cuervo, J., Lee, T., & Tsontos, V. M. (2013). Aquarius and SMOS detect effects of an extreme Mississippi River flooding event in the Gulf of Mexico. *Geophysical Research Letters*, *40*(19), 5188–5193. https://doi.org/10.1002/grl.50995

Giffard, P., Llovel, W., Jouanno, J., Morvan, G., & Decharme, B. (2019). Contribution of the Amazon River discharge to regional sea level in the tropical Atlantic ocean. *Water*, *11*, 2348. https://doi.org/10.3390/w11112348

Gittings, S. (2016). https://sanctuaries.noaa.gov/news/jul16/noaa-scientists-report-mass-die-off-of-invertebrates-at-east-flower-garden-bank.html

Han, W., & Webster, P. (2002). Forcing mechanisms of sea level interannual variability in the Bay of Bengal. *Journal of Physical Oceanography*, *32*, 216–239. https://doi.org/10.1175/1520-0485(2002)032<0216:FMOSLI>2.0.CO;2

Hernandez, O., Jouanno, J., & Durand, F. (2016). Do the Amazon and Orinoco freshwater plumes really matter for hurricane-induced ocean surface cooling? *Journal of Geophysical Research: Oceans*, *121*, 2119–2141. https://doi.org/10.1002/2015JC011021

Hickey, B. M., Kudela, R. M., Nash, J. D., Bruland, K. W., Peterson, W. T., MacCready, P., et al. (2010). River influences on shelf ecosystems: Introduction and synthesis. *Journal of Geophysical Research*, *115*, C00B17. https://doi.org/10.1029/2009JC005452

Holt, J., Hyder, P., Ashworth, M., Harle, J., Hewitt, H. T., Liu, H., et al. (2017). Prospects for improving the representation of coastal and shelf seas in global ocean models. *Geoscientific Model Development*, *10*(1), 499–523. https://doi.org/10.5194/gmd-10-499-2017

Horner-Devine, A. R., Hetland, R. D., & MacDonald, D. G. (2015). Mixing and transport in coastal river plumes. *Annual Review of Fluid Mechanics*, *47*, 569–594. https://doi.org/10.1146/annurev-fluid-010313-141408

Hua, W., Zhou, L., Nicholson, S. E., Chen, H., & Qin, M. (2019). Assessing reanalysis data for understanding rainfall climatology and variability over Central Equatorial Africa. *Climate Dynamics*, *53*(1–2), 651–669. https://doi.org/10.1007/s00382-018-04604-0

Large, W. G., & Yeager, S. G. (2009). The global climatology of an interannually varying air-sea flux data set. *Climate Dynamics*, *33*(2–3), 341–364. https://doi.org/10.1007/s00382-008-0441-3

Lee, K., Tong, L. T., Millero, F. J., Sabine, C. L., Dickson, A. G., Goyet, C., et al. (2006). Global relationships of total alkalinity with salinity and temperature in surface waters of the world's oceans. *Geophysical Research Letters*, *33*(19), L19605. https://doi.org/10.1029/2006GL027207

Lee, T. (2016). Consistency of Aquarius sea surface salinity with argo products on various spatial and temporal scales. *Geophysical Research Letters*, *43*(8), 3857–3864. https://doi.org/10.1002/2016GL068822

Lee, T., Fournier, S., Gordon, A. L., & Sprintall, J. (2019). Maritime Continent water cycle regulates low-latitude chokepoint of global ocean circulation. *Nature Communications*, *10*. https://doi.org/10.1038/s41467-019-10109-z

Marcello, P., Müller, F. L., Oelsmann, J., Rautiainen, L., Dettmering, D., Hart-Davis, M. G., et al. (2021). Absolute Baltic sea level trends in the satellite altimetry era: A revisit. *Frontiers in Marine Science*, *8*, 546. ISSN=2296-7745. https://doi.org/10.3389/fmars.2021.647607

Marshall, J., Adcroft, A., Hill, C., Perelman, L., & Heisey, C. (1997). A finite-volume, incompressible Navier Stokes model for studies of the ocean on parallel computers. *Journal of Geophysical Research*, *102*(C3), 5753–5766. https://doi.org/10.1029/96JC02775

Marshall, J., Hill, C., Perelman, L., & Adcroft, A. (1997). Hydrostatic, quasi-hydrostatic, and nonhydrostatic ocean modeling. *Journal of Geophysical Research*, *102*(C3), 5733–5752. https://doi.org/10.1029/96JC02776

Meade, R. H., & Emery, K. O. (1971). Sea level as affected by river runoff, Eastern United States. *Science*, *173*(3995), 425–428. https://doi.org/10.1126/science.173.3995.425

Meissner, T., Wentz, F., Manaster, A., & Lindsey, R. (2019). *NASA/RSS SMAP salinity: Version 4.0 validated release*. Retrieved from https://podaac-tools.jpl.nasa.gov/drive/files/allData/smap/docs/V4/RSS_SMAP-SSS_V4.0_TechnicalDocumentation.pdf

Newinger, C., & Toumi, R. (2015). Potential impact of the colored Amazon and Orinoco plume on tropical cyclone intensity. *Journal of Geophysical Research: Oceans*, *120*, 1296–1317. https://doi.org/10.1002/2014JC010533

Piecuch, C. G., Bittermann, K., Kemp, A. C., Ponte, R. M., Little, C. M., Engelhart, S. E., & Lentz, S. J. (2018). River-discharge effects on United States Atlantic and Gulf coast sea-level changes. *Proceedings of the National Academy of Sciences of the United States of America*, *115*(30), 7729–7734. https://doi.org/10.1073/pnas.1805428115

Piecuch, C. G., & Wadehra, R. (2020). Dynamic sea level variability due to seasonal River discharge: A preliminary global ocean model study. *Geophysical Research Letters*, *47*(4), e2020GL086984. https://doi.org/10.1029/2020GL086984

Rabalais, N. N., Turner, R. E., Justic, D., Dortch, Q., & William, J. W. (1999). Ecological and economic consequences of hypoxia: Topic 2 report for the integrated assessment on hypoxia in the Gulf of Mexico. In *NOAA coastal ocean program decision analysis series No. 15* (Vol. 167). NOAA Coastal Ocean Program.

Redi, M. H. (1982). Oceanic isopycnal mixing by coordinate rotation. *Journal of Physical Oceanography*, *12*(10), 1154–1158. https://doi.org/10.1175/1520-0485(1982)012<1154:OIMBCR>2.0.CO;2

Reul, N., Fournier, S., Boutin, J., Hernandez, O., Maes, C., Chapron, B., et al. (2014). Sea surface salinity observations from space with the SMOS satellite: A new means to monitor the marine Branch of the water cycle. *Surveys in Geophysics*, *35*(3), 681–722. https://doi.org/10.1007/s10712-013-9244-0

Reul, N., Quilfen, Y., Chapron, B., Fournier, S., Kudryavtsev, V., & Sabia, R. (2014). Multisensor observations of the Amazon-Orinoco river plume interactions with hurricanes. *Journal of Geophysical Research: Oceans*, *119*(12), 8271–8295. https://doi.org/10.1002/2014JC010107

Sprintall, J., & Tomczak, M. (1992). Evidence of the barrier layer in the surface layer of the tropics. *Journal of Geophysical Research*, *97*(C5), 7305. https://doi.org/10.1029/92jc00407

Sun, Q., Whitney, M. M., Bryan, F. O., & Tseng, Y.-H. (2017). A box model for representing estuarine physical processes in Earth system models. *Ocean Modelling*, *112*, 139–153. https://doi.org/10.1016/j.ocemod.2017.03.004

Sun, Q., Whitney, M. M., Bryan, F. O., & Tseng, Y.-H. (2019). Assessing the skill of the improved treatment of riverine freshwater in the Community Earth System Model (CESM) relative to a new salinity climatology. *Journal of Advances in Modeling Earth Systems*, *11*(5), 1189–1206. https://doi.org/10.1029/2018MS001349

Suzuki, T., Yamazaki, D., Tsujino, H., Komuro, Y., Nakano, H., & Urakawa, S. (2018). A dataset of continental river discharge based on JRA-55 for use in a global ocean circulation model. *Journal of Oceanography*, *74*(4), 421–429. https://doi.org/10.1007/s10872-017-0458-5

Tang, W., Yueh, S., Yang, D., Fore, A., Hayashi, A., Lee, T., et al. (2018). The potential and challenges of using Soil Moisture Active Passive (SMAP) sea surface salinity to monitor Arctic Ocean freshwater changes. *Remote Sensing*, *10*(6), 869. https://doi.org/10.3390/rs10060869

Tsujino, H., Urakawa, L. S., Griffies, S. M., Danabasoglu, G., Adcroft, A. J., Amaral, A. E., et al. (2020). Evaluation of global ocean-sea-ice model simulations based on the experimental protocols of the Ocean Model Intercomparison Project phase 2 (OMIP-2). *Geoscientific Model Development Discussions*, *13*, 1–86. https://doi.org/10.5194/gmd-13-3643-2020

Tsujino, H., Urakawa, S., Nakano, H., Small, R. J., Kim, W. M., Yeager, S. G., et al. (2018). JRA-55 based surface dataset for driving ocean-sea-ice models (JRA55-do). *Ocean Modelling*, *130*, 79–139. https://doi.org/10.1016/j.ocemod.2018.07.002

Vignudelli, S., Birol, F., Benveniste, J., Fu, L.-L., Picot, N., Raynal, M., & Roinard, H. (2019). Satellite altimetry measurements of sea level in the coastal Zone. *Surveys in Geophysics*, *40*, 1319–1349. https://doi.org/10.1007/s10712-019-09569-1

Vinogradova, N., Lee, T., Boutin, J., Drushka, K., Fournier, S., Sabia, R., et al. (2019). Satellite salinity observing system: Recent discoveries and the way forward. *Frontiers in Marine Science*, *6*. https://doi.org/10.3389/fmars.2019.00243

Vizy, E. K., & Cook, K. H. (2010). Influence of the Amazon/Orinoco plume on the summertime Atlantic climate. *Journal of Geophysical Research*, *115*(21), D21112. https://doi.org/10.1029/2010JD014049

Vu, P. L., Frappart, F., Darrozes, J., Marieu, V., Blarel, F., Ramillien, G., et al. (2018). Multi-satellite altimeter validation along the French Atlantic coast in the southern Bay of Biscay from ERS-2 to SARAL. *Remote Sensing*, *10*(1), 93. https://doi.org/10.3390/rs10010093

Washington, R., James, R., Pearce, H., Pokam, W. M., & Moufouma-Okia, W. (2013). Congo basin rainfall climatology: Can we believe the climate models? *Philosophical Transactions of the Royal Society B: Biological Sciences*, *368*(1625), 20120296. https://doi.org/10.1098/rstb.2012.0296

Wu, Q., Wang, X., Liang, W., & Zhang, W. (2020). Validation and application of soil moisture active passive sea surface salinity observation over the Changjiang River Estuary. *Acta Oceanologica Sinica*, *39*, 1–8. https://doi.org/10.1007/s13131-020-1542-z

Wunsch, C., & Heimbach, P. (2013). Dynamically and kinematically consistent global ocean circulation and ice state estimates. *International Geophysics*, *103*, 553–579. https://doi.org/10.1016/B978-0-12-391851-2.00021-0

Wunsch, C., Heimbach, P., Ponte, R. M., & Fukumori, I. (2009). The global general circulation of the ocean estimated by the ECCO-Consortium. *Oceanography*, *22*, 88–103. https://doi.org/10.5670/oceanog.2009.41

Zhang, H., Menemenlis, D., & Fenty, I. G. (2018). *ECCO LLC270 ocean-ice state estimate* (Vol. 7). Retrieved from http://hdl.handle.net/1721.1/119821